Z-Scheme g-C3N4/Fe3O4/Ag3PO4 @Sep magnetic nanocomposites as heterojunction photocatalysts for green malachite degradation and dynamic molecular studies

R. Haounati, H. Ighnih, H. Ouachtak, Rahime Eshaghi Malekshah, N. Hafid, A. Jada, A. Ait Addi

To cite this version:

R. Haounati, H. Ighnih, H. Ouachtak, Rahime Eshaghi Malekshah, N. Hafid, et al.. Z-Scheme g-C3N4/Fe3O4/Ag3PO4 @Sep magnetic nanocomposites as heterojunction photocatalysts for green malachite degradation and dynamic molecular studies. Colloids and Surfaces A: Physicochemical and Engineering Aspects, 2023, 671, pp.131509. 10.1016/j.colsurfa.2023.131509 . hal-04297898

HAL Id: hal-04297898
https://hal.science/hal-04297898

Submitted on 22 Nov 2023

Z-Scheme g-C_3N_4/Fe_3O_4/Ag_3PO_4@Sep magnetic nanocomposites as heterojunction photocatalysts for green malachite degradation and Dynamic molecular studies

R. Haounati [1], *, H. Ighnih [1], H. Ouachtak [1,2],*, Rahime Eshaghi Malekshah [3] , N. Hafid [4] , A. Jada [5,6],* , A. Ait addi [1]

[1] Physical Chemistry & Environment Team, Faculty of Sciences, Ibn Zohr University, Agadir, Morocco.

[2] Department of Applied Chemistry, Faculty of Applied Sciences, Ibn Zohr University, Ait Melloul, Morocco.

[3] Medical Biomaterial Research Centre (MBRC), Tehran University of Medical Sciences, Tehran, Iran

[4] Center For Education & Training Profession Souss Massa, Morocco.

[5] Institute of Materials Science of Mulhouse (IS2M), Haute Alsace University,Mulhouse 68100, France.

[6] Strasbourg University, Strasbourg 67081, France.

*Corresponding authors:

amane.jada@uha.fr ; ouachtakhassan@gmail.com ; haounati.redouane@gmail.com

Graphical abstract

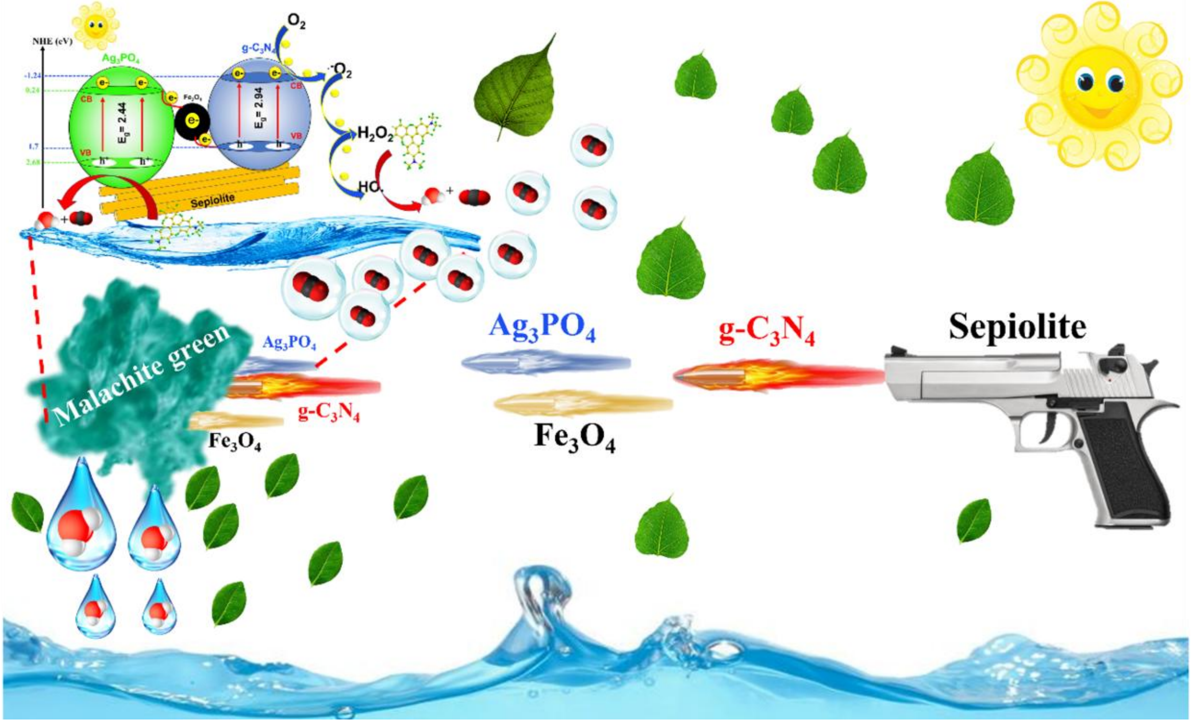

Abstract

Recently, the synthesis of Z-scheme nanocomposite heterojunctions has received significant attention. In the present work, we prepared a Z-scheme heterostructures nanocomposite by using a facile co-precipitation method. Several techniques were used to characterize the structures, the morphologies, the optical and the electronic properties, as well as the photocatalytic performance of the nanocomposite. Thus, the scanning electron microscope and the transmission electron microscope analyses showed that the sepiolite surface was well occupied by the Ag_3PO_4, the g-C_3N_4 and the Fe_3O_4 nanoparticles. Further, the g-C_3N_4/Fe_3O_4/Ag_3PO_4@Sep nanocomposite, as compared to pure g-C_3N_4, g-C_3N_4@Sep and g-C_3N_4/Ag_3PO_4@Sep, exhibited significantly improved photocatalytic performance for the degradation of malachite green (MG) (100%, 12 min). Such photocatalytic activity was found to be about □27, 26 and 1.85 times higher than that of g-C_3N_4, g-C_3N_4@Sep and g-C_3N_4/Ag_3PO_4@Sep, respectively. The photocatalytic enhancement of magnetic nanocomposite g-C_3N_4/Fe_3O_4/Ag_3PO_4@Sep to degrade organic molecules such as MG dye, under solar light irradiation, was attributed to the synergy effects between Ag_3PO_4 supported by sepiolite clay and g-C_3N_4 combined with the Fe_3O_4 nanoparticles. Furthermore, the photocatalytic activity of g-C_3N_4/Fe_3O_4/Ag_3PO_4@Sep remained at a high level even after four cycles, suggesting that the quaternary nanocomposite has a high stability and good reusability, as resulting from the suitable band structure and the Z-scheme heterojunction construction, which improved the light usage and the charge carrier migration rate. DFT-D correction was used to optimize all the structures. Then, MD calculations were applied to form Fe_3O_4/Ag_3PO_4@Sep nano-composite, resulting the stable configuration due to the negative adsorption. At last, the MG adsorption was investigated by adsorption locator module on nano-composite, suggesting the thermodynamic stability system.

Keywords: Z-scheme, nanocomposite, malachite green, MD calculation.

1. Introduction

In the recent years, the aquatic systems pollution has led to several humans and animals health issues, impacting the economy and affecting the climate change [1–4]. Such water pollution results mainly from the growing industrialization and the agricultural activities, and leads to wastewater large amounts production [5]. The polluted waters may contain toxic metals, organic molecules, dyes and drugs [6]. Particularly, the dye effluents originating from textile, leather, cosmetics and pigments industries, are responsible for one of the major water pollution problems in the world, and they should be consequently investigated [7].

Several methods such as the physical adsorption [8, 9], the biological process [10], and the chemical oxidation [11, 12], have been applied at laboratory, as well as, at large scales, for the wastewater treatment and the dye removal from the contaminated aqueous medium. Among these methods, the Advanced Oxidation Processes (AOP), such as: photocatalytic degradation using heterogeneous photocatalytic process, has been found to be a superior method, due to its operational simplicity, its high efficiency toward the organic dyes, its economic benefits and its facile mineralization of organic dyes into H_2O and CO_2 [13]. On the other hand, various materials used as adsorbents and/or catalysts, for the dye removal from wastewaters using the AOP method, they mainly include few high surface area materials such as zeolite, activated carbon, carbon nanotubes, graphene and some other photocatalytic materials such as oxides (ZnO, Bi_2O_3, TiO_2, YVO_4, WO_3), hydroxides ($La(OH)_3$), sulfurs (MoS_2) and phosphates ($BiPO_4$, $CePO_4$, Ag_3PO_4) [13, 14]. For the silver orthophosphate (Ag_3PO_4) based semiconductor photocatalysts, due to their strong oxidation abilities, and their non-toxicities, they have been widely employed for water purification [15]. In addition, to enhance the catalytic activity of these silver orthophosphate (Ag_3PO_4) based materials, several modifications were realized, including: homojunction construction, Z-Scheme composite design, and defect generation [16]. The Z-Scheme design consist on improving the separation efficiency of photogenerated electron(-)-hole(+) pairs by constructing heterojunction Z-scheme photocatalysts with typical n-type semiconductors, such as: CeO_2, TiO_2, Fe_2O_3, ZnO, etc.[13]. There are many problems associated with Z-scheme photocatalysts materials, including the problem of charge transport at incomplete contact interfaces [17], and the sufferance from the recycling process [13].

The present work deals with novel “g-C_3N_4 /Fe_3O_4 /Ag_3PO_4@Sep” Z-scheme based photocatalysts, which were prepared, using a simple co-precipitation approach, to enhance the sunlight degradation of Malachite Green MG dye in water. To the best of our knowledge, there are no reported work on the preparation and the application of this material in the photocatalytic decomposition performance of dyes under sunlight irradiation.

In the Z-scheme based photocatalyst preparation, the Fe_3O_4 was used as an n-type semiconductor, due to its strong magnetic properties, the sepiolite clay (having the chemical formula: $Mg_4Si_6O_{15}(OH)_2 \cdot 6H_2O$) was used for its important benefits (environmentally friendly, stable, inexpensive), and its large specific surface area, the g-C_3N_4 was used since it is considered as a major component in the design of new photocatalysts for photodegradation of organic molecules such as dyes under sunlight irradiation. The high photocatalytic activity of the g-C_3N_4can be explained by its band gap of 2.7 eV, yielding to an absorption edge suitable for visible light capture, and band positions suitable for water oxidation-reduction, and leading to high thermal and chemical stabilities[18, 19].It should be noted that the sepiolite can provide more active sites for the Z-scheme “g-C_3N_4/Fe_3O_4/Ag_3PO_4” photocatalyst.

In the present work, the structure and the morphology of the elaborated photocatalysts were investigated. Further, we propose a possible enhanced Z-scheme heterojunction mechanism of electron transfer. MD simulation was used to form Fe_3O_4/Ag_3PO_4@Sep nano-composite and MG adsorption on this nano-composite.

2. Experimental

2.1. Samples preparation

2.1.1. Chemicals

The raw clay used in this work is sepiolite (Sep), is the same as used elsewhere [20].The other chemicals, including melamine ($C_3H_6N_6$, 99%), ferric chloride hexahydrate ($FeCl_3 \cdot 6H_2O$, 97%), ferrous sulfate hepta hydrate ($FeSO_4.7H_2O$, 99%), silver nitrate ($AgNO_3$, 99.8%), ammonium dihydrogen phosphate ($NH_4H_2PO_4$, 98%),hydrochloric acid (HCl, 99%), sodium hydroxide (NaOH, 98%), malachite green (MG, 99%) and ethylene glycol ($HOCH_2CH_2OH$, 99%), were all of analytical grade, purchased from Sigma-Aldrich and used as received.

2.1.2 Synthesis of g-C_3N_4 and Fe_3O_4

The g-C_3N_4 photocatalyst was synthesized through simple melamine calcination, by heating, at 550 °C for 3 h (heating rate of 5 °C/min) 5g of melamine powder, and by using an alumina crucible placed in a muffle furnace, as depicted in **Figure.1**.

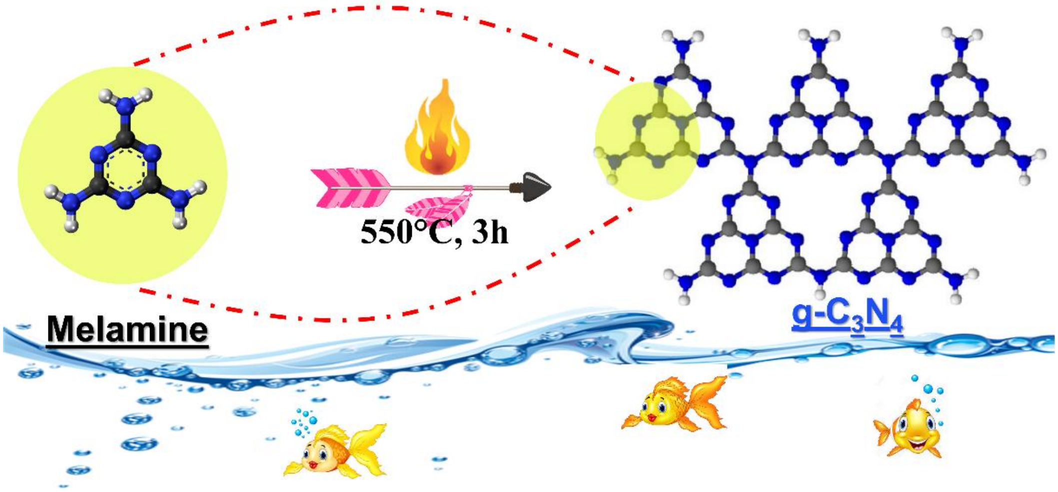

Figure. 1: Mechanism of g-C_3N_4 preparation from melamine

The magnetite Fe_3O_4 was prepared by co-precipitation method. Thus, in typical experiment, 4.670 g of $FeCl_3.6H_2O$ and 2.401 g of $FeSO_4.7H_2O$ were dissolved in 50 ml of ethylene glycol/deionized water with the ratio 1/1 under vigorous magnetic stirrer at room temperature for 30 min under N_2. Then amounts of NaOH 1M solution were added dropwise to the previous solution, under constant magnetic stirring to adjust the pH to 9. Afterwards, the mixture was magnetically stirred for 12 h more. Subsequently, the obtained mixture was washed with distilled water, and the resulting black Fe_3O_4 was dried at 80 °C for 24 h as shown in **Figure.2**.

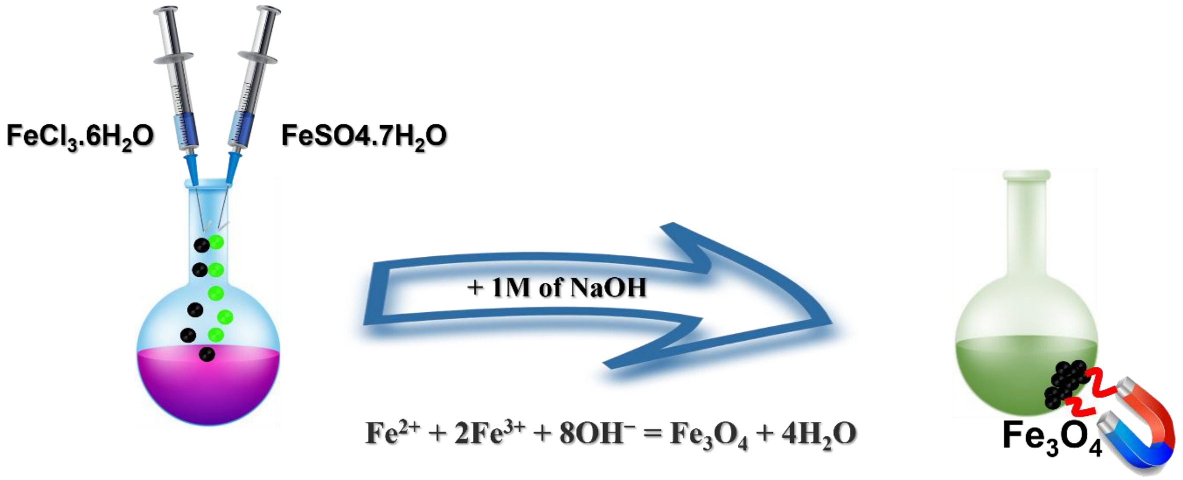

Figure. 2: The scheme for the Fe_3O_4 nanoparticles formation

2.1.3 Synthesis of quaternary g-C_3N_4/Fe_3O_4/Ag_3PO_4@Sep nanocomposites

The g-C_3N_4/Fe_3O_4/Ag_3PO_4@Sep nanocomposite was prepared by a facile heterogeneous suspension reaction procedure.

Firstly, the sepiolite-supported-Ag_3PO_4(Ag_3PO_4@Sep) nanocomposite was synthesized through a simple electrostatically driven reaction. Thus, in a typical experimental synthesis procedure, a sepiolite suspension was obtained by dispersing 4 g of the raw sepiolite in 200 mL of distilled water using ultrasonic treatment. Afterwards, a solution of $AgNO_3$ was added dropwise to the aqueous sepiolite dispersion in order to recover totally the negatively charged sepiolite sheets by the positive Ag^+ charges. Subsequently, 0.048 mM $NH_4H_2PO_4$ was added, drop by drop, to the sepiolite-$AgNO_3$ mixture and NaOH 0.5M was slowly added into the resulting mixture, followed by magnetic stirring at room temperature for 4 h. At the end of the reaction, a green-yellow precipitate of Ag_3PO_4@Sep was recovered by centrifugation at 5000 rpm for 10 min, washed several times with distilled water, and dried at 80 °C overnight.

Secondly, the magnetic nanocomposite (Fe_3O_4/Ag_3PO_4@Sep) was prepared by dropping off Fe_3O_4 nanoparticles (10 mg/mL) on the surface of the heterogeneous Ag_3PO_4@Sep suspension, under vigorous stirring for 4 h. The resulting magnetic nanocomposite Fe_3O_4/Ag_3PO_4@Sep was collected by a permanent magnet, washed with distilled water multiple times, and dried under vacuum overnight. In the last step, a g-C_3N_4 suspension was dropped off the surface of the Fe_3O_4/Ag_3PO_4@Sep nanocomposite. Finally, the obtained magnetic nanocomposite was separated by a permanent magnet and washed several times by deionized water, and then dried at 80°C.The obtained sample was denoted as g-$C_3N_4/Fe_3O_4/Ag_3PO_4$@Sep. **Figure. 3** shows the steps involved in the magnetic g-$C_3N_4/Fe_3O_4/Ag_3PO_4$@Sep nanocomposite synthesis.

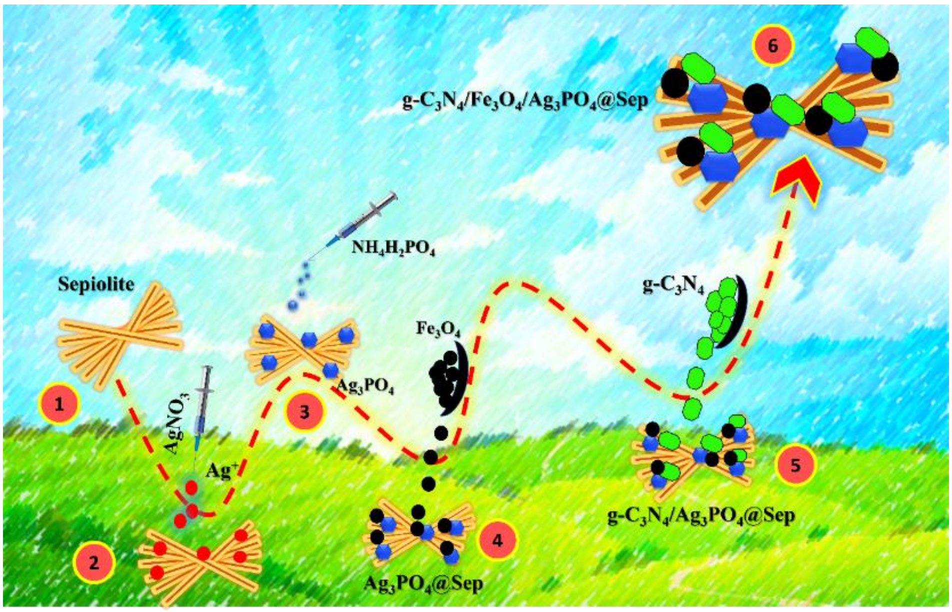

Figure. 3: The formation mechanism of quaternary g-$C_3N_4/Fe_3O_4/Ag_3PO_4$@Sep

2.2. Photocatalytic activity

The photocatalytic activity of the g-C_3N_4, Ag_3PO_4, Fe_3O_4, Ag_3PO_4@Sep and g-$C_3N_4/Fe_3O_4/Ag_3PO_4$@Sep nanocomposite photocatalysts were evaluated for the photodegradation of Malachite Green (MG) in aqueous media under sunlight irradiation. Hence, in typical photocatalytic experiment, an amount of 100 mg of the photocatalyst was dispersed in 100 mL MG dye solution (10 mg/L). The prepared suspensions were maintained inside the reactor, in the dark, for 1 h to reach an adsorption-desorption equilibrium between the support and MG dye molecules, then 5 mL solutions were withdrawn every 2 minutes under sunlight irradiation. Subsequently, the solution was centrifuged to separate the liquid and solid phases for determine the concentration of MG dye with the wavelength of 615 nm using UV visible JENWAY-6705 spectrophotometer. The percent degradation was measured using the expression (**Eq.1**):

$$\%\ \text{of dye degradation} = \frac{C_0 - C_t}{C_0} \times 100 \qquad (1)$$

where C_0 is the original absorbance value of MG dye at initial time, and C_t is the absorbance value of MG dye at a given time after sunlight irradiation.

2.3. Computational details

$Mg_4Si_6O_{15}(OH)_2{\cdot}6H_2O$ (sepiolite like palygorskite: Sep) with lattice parameters a = 13.5, b = 27.0, and c = 5.30 Å and built based on (200) surface and thickness of 1.574 Å (**Figures 4a-b**) [21]. C_3N_4, Ag_3PO_4 and MG (malachite green) was used to perform all the required calculations based on Density functional theory (DFT-D) by $DMol^3$ module, GGA/ PBE functional and DND and spin-unrestricted in Materials Studio 2017 software (**Figures 4c-d**). Fe_3O_4 as cubic (ID: mp-753222 and Point Group $Fd\bar{3}m$) with $a = b = c = 8.44$ Å, $\alpha = \beta = \gamma = 90.00°$ and volume of 602.06 $Å^3$ was downloaded from https://materialsproject.org/materials/mp-19306 (Figures 4e-f). After that, Fe_3O_4 without unitcell was made based on (220) surface and thickness of 1.500 Å and slab position (1.00) (**Figure 4g**). In order construct nano-composite $Fe_3O_4/Ag_3PO_4@Sep$, dynamic calculation (by the Monte Carlo adsorption locator module) was used to assess the adsorption of 6 C_3N_4, Ag_3PO_4 and Fe_3O_4 molecules [22].Additionally, 6 molecules of MG were adsorbed on Ag_3PO_4($Ag_3PO_4@Sep$ by the Monte Carlo adsorption locator module [23].

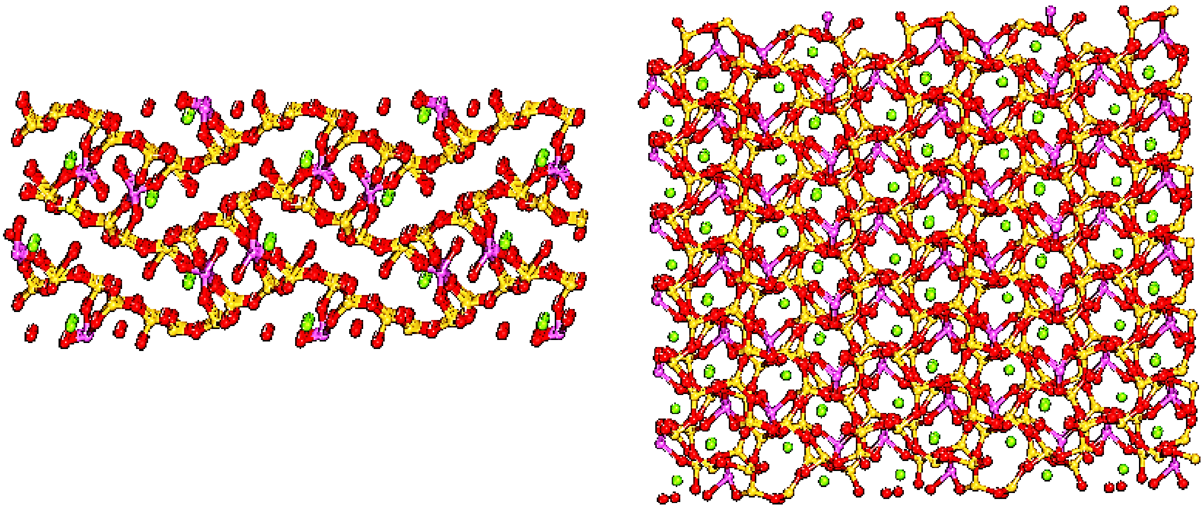

a **b**

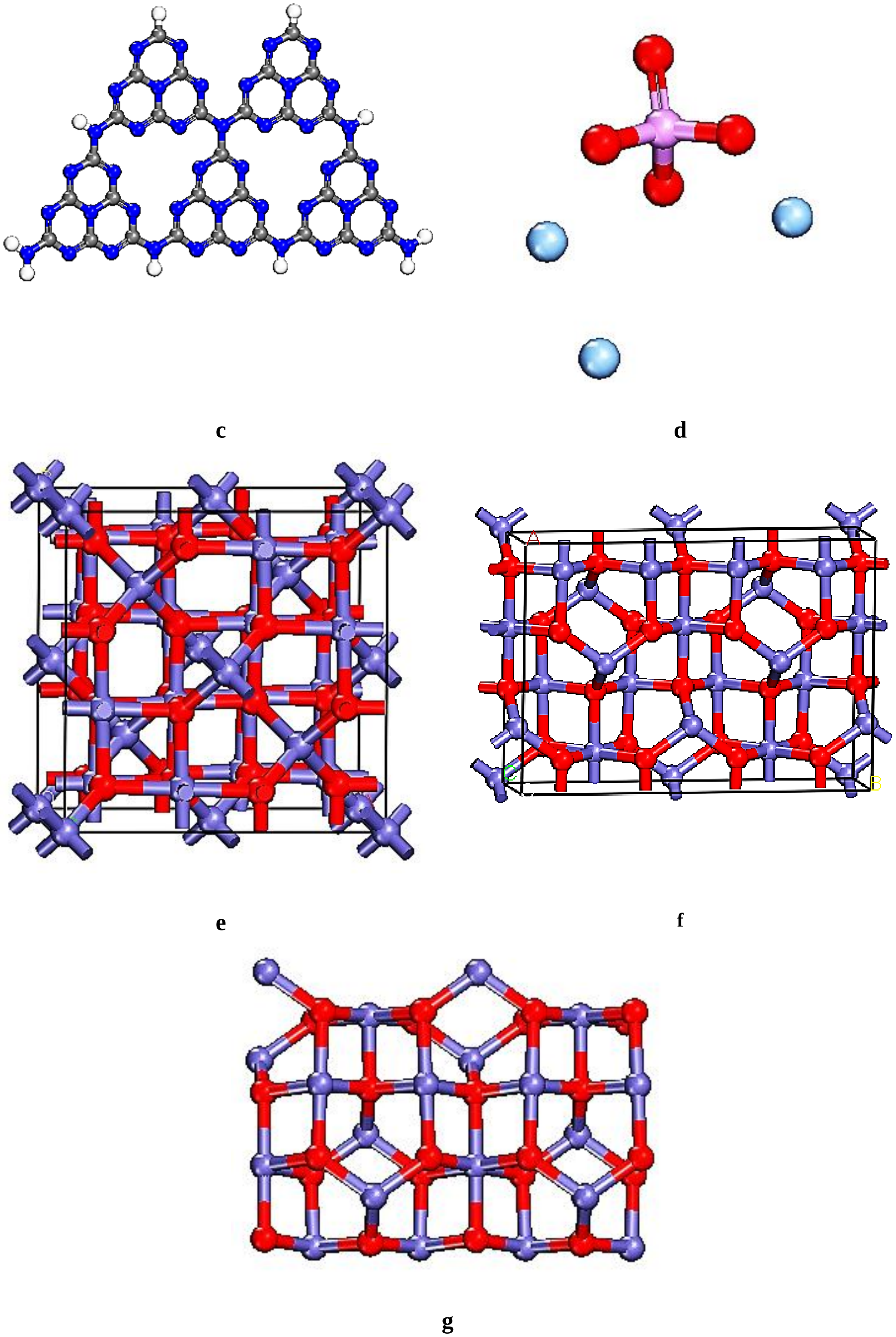

c

d

e

f

g

Figure 4. Snapshots of the optimized structures (a and b); $Mg_4Si_6O_{15}(OH)_2\cdot 6H_2O$ (sepiolite,

(c); C_3N_4, (d); Ag_3PO_4, (e); Fe_3O_4 as cubic (ID: mp-753222), (f); Fe_3O_4 (220) and (g); Fe_3O_4 (220) without unicell. Colored balls are Mg (green), oxygen (red), orange (Si), violet (Fe), pink (Al), and white (H).

3. Results and discussion

3.1. Characterizations of the g-C_3N_4/Fe_3O_4/Ag_3PO_4@Sep nanocomposites

XRD analyzes

The crystalline structures of the as-prepared samples were determined by XRD. Thus, **Figure. 5** shows the XRD patterns of pure g-C_3N_4, sepiolite, Fe_3O_4 and g-C_3N_4/Fe_3O_4/Ag_3PO_4@Sep nanocomposites.

Two distinct fundamental diffraction peaks are shown for the g-C_3N_4 sample, the great peak located at ~ 27.4° corresponds to (0 0 2) planes and it is due to the stacking of the conjugated double bonds with the interlayer d-spacing (0.336 nm), while the small peak at~13.1°, is indexed as (1 0 0) planes, and it is attributed to the interplanar of interlayer d-spacing (0.672 nm) [24]. For the sepiolite clay, all the observed diffraction peaks of the sample were found to correspond to the JCPDS card (No. 75–1597) in addition to the observed few peaks resulting from quartz and carbonates impurities. The characteristic diffraction peaks of the synthesized Fe_3O_4 nanoparticles occurred at diffraction angles, $2\theta = 30.46^{\circ}$, 35.60°, 43.48°, 53.84°, and $57.40,^{\circ}$ which are attributed to (2 2 0), (3 1 1), (4 0 0), (4 2 2), and (5 1 1) planes, respectively, confirming the formation of the Fe_3O_4 spinel cubic phase (JCPDS No. 01–076-0955).Finally, the X-ray diffraction (XRD) pattern of the g-C_3N_4/Fe_3O_4/Ag_3PO_4@Sep nanocomposite shows clearly all the diffraction peaks of Ag_3PO_4 which can be easily indexed to the Ag_3PO_4centered cubic structure and correspond to the JCPDS card (No. 06-0505).As can be seen also in **Figure. 5**, the XRD spectrum of the nanocomposite shows the presence of the sepiolite and the body cubic spinel Fe_3O_4 nanoparticles peaks, which confirm the successful preparation of g-C_3N_4/Fe_3O_4/Ag_3PO_4@Sep nanocomposite.

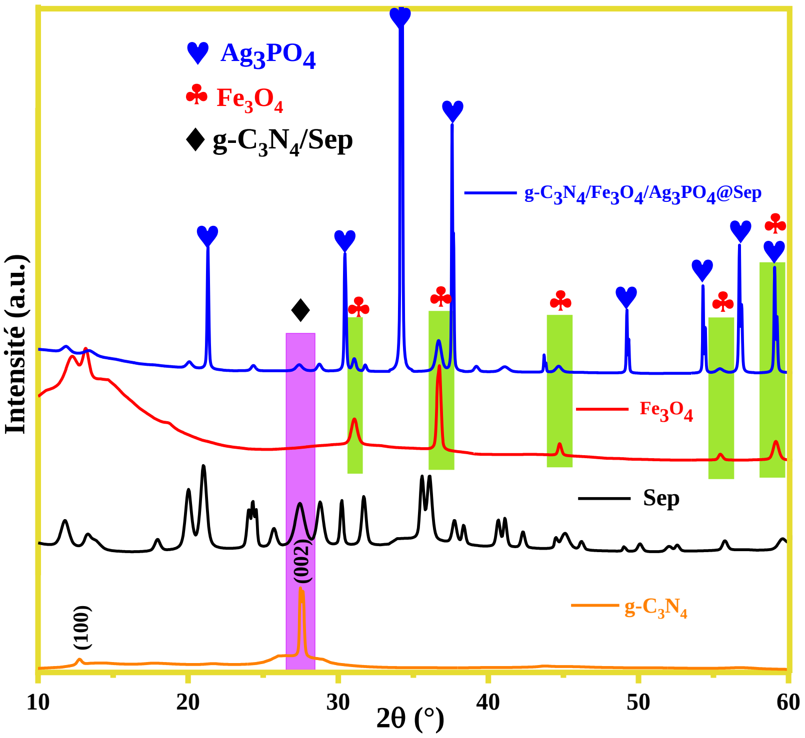

Figure. 5. XRD patterns of the prepared samples.

FTIR analyzes

In order to assess the successful formation of nanocomposites, FTIR spectroscopy was used as a tool to investigate the chemical structures of the various prepared samples. Thus, **Figure. 6** shows the FTIR spectra of g-C_3N_4, Sepiolite, Fe_3O_4, Ag_3PO_4@Sep and g-C_3N_4/Fe_3O_4/Ag_3PO_4@Sep catalysts. As can be seen in **Figure. 6a**, the g-C_3N_4 sample shows strong IR responses. In this figure, the bands located at 1251, 1325, 1419, 1571, and 1639 cm^{-1} could be attributed to the typical stretching modes of CN heterocycles, whereas the absorption peaks at 800 cm^{-1} and 889 cm^{-1} are ascribed to the typical breathing mode of tri-s-triazine units and the deformation mode of N – H bonds, respectively [25, 26]. For the sepiolite, the FTIR spectrum depicted in **Figure. 6b** exhibits two absorption peaks of zeolitic water (3433 cm^{-1} and 1644 cm^{-1}) and coordinated water (3581 cm^{-1}) present in the sepiolite nanofibers structure. Note that the absorption peaks located in the region of 788–675 cm^{-1}, were attributed to the bending and the stretching vibration of hydroxyl groups (Mg-OH), whereas the band located at 1016 cm^{-1}, 455 cm^{-1}, 1215 cm^{-1} and 1074 cm^{-1},they might be due to the Si-O bonds stretching[27, 28]. For the Fe_3O_4 nanoparticles spectrum, as shown in **Figure. 6c**, two characteristic peaks located at 556 cm^{-1} and 1058 cm^{-1}were observed, corresponding to the Fe–O stretching mode in the Fe_3O_4confirming that the main phase is magnetite[29].In the case of Ag_3PO_4@Sep, as can be seen in **Figure. 6d**,the spectrum shows, in addition to all characteristic peaks of raw sepiolite, three characteristic bands located at 1012 cm^{-1}, 1012 cm^{-1} and 1390 cm^{-1}, due to stretching vibration and bending vibration of P-O-P and P=O of pure Ag_3PO_4[29].

For the g-C_3N_4/Fe_3O_4/Ag_3PO_4@Sep nanocomposite FTIR spectrum shown in **Figure. 6e**, as can be observed, the presence of all the characteristic bands of sepiolite, Fe_3O_4, Ag_3PO_4 and g-C_3N_4, confirms that Ag_3PO_4 nanoparticles cover the sepiolite surface of and they are joined to the g-C_3N_4 nano sheets by Fe_3O_4 nanoparticles. Thus, from the overall FTIR data, the successfully preparation of the g-C_3N_4/Fe_3O_4/Ag_3PO_4@Sep nanocomposite is clearly evidenced.

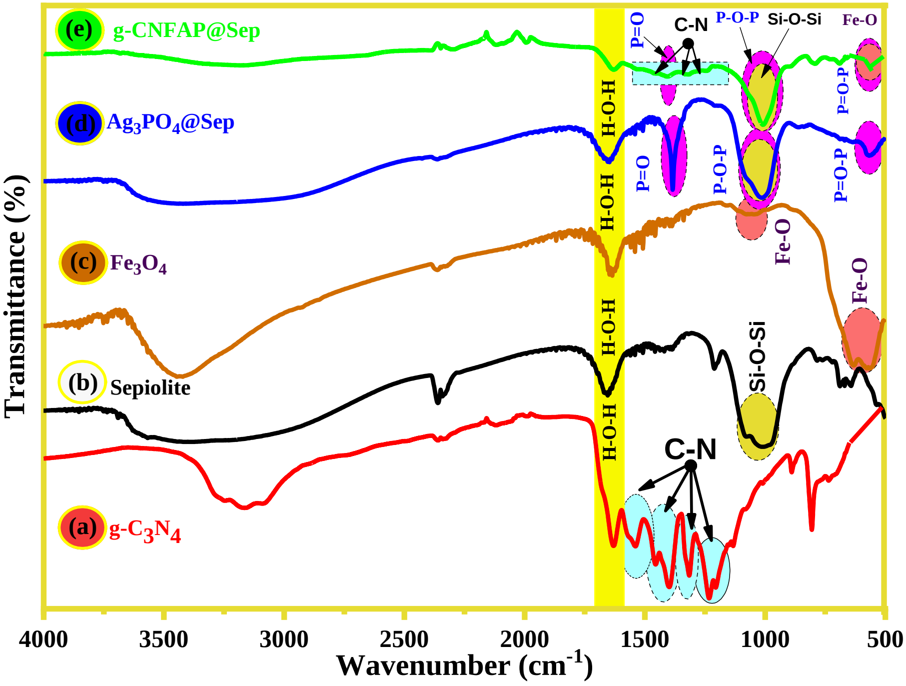

Figure. 6. FTIR spectra of photocatalysts. (a) g-C_3N_4, (b) Sepiolite, (c) Fe_3O_4, (d) Ag_3PO_4/Sep and (e) g-C_3N_4/Fe_3O_4/Ag_3PO_4@Sep.

SEM analyzes

The surface structure and morphological characteristics of g-C_3N_4, Sepiolite, Ag_3PO_4@Sep and g-C_3N_4/Fe_3O_4/Ag_3PO_4@Sep the composites were investigated using SEM as shown in **Figure.7**.The g-C_3N_4(**Figure. 7a)** prepared directly from the calcination of the melamine shows a mesoporous structure with an irregular sheet shape**.** It can be observed from **Figure. 7b** that the raw sepiolite surface reveals compact nodular with non-uniform fibrous filament morphology. After surface modification of sepiolite by Ag_3PO_4 nanoparticles, as shown in **Figure. 7c**, it is obvious that the Ag_3PO_4 slightly changes the raw sepiolite by making the nanofibrous surface rougher. Note that the Ag_3PO_4 nanoparticles attachment on the sepiolite surface results from the electrostatic interaction. In addition, the image in **Figure. 7c** shows small particle sizes with sheets shapes, which are attributed to g-C_3N_4. According to the SEM image of g-C_3N_4/Fe_3O_4/Ag_3PO_4@Sep nanocomposite shown in **Figure. 7d**, the Fe_3O_4 nanoparticles, the Ag_3PO_4 nanoscale and the g-C_3N_4 nanosheets are homogeneously distributed, and cover all the sepiolite fibrous surface. In summary, the obtained SEM images show high adhesion of the prepared catalysts, mainly Ag_3PO_4particles on the sepiolite surface, which may increase the nano composite photogenerated carriers' lifetime.

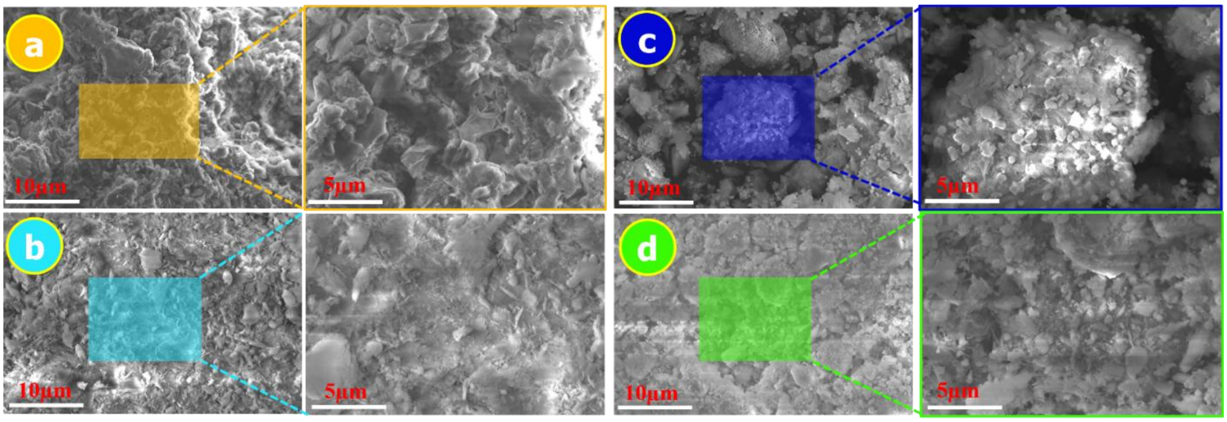

Figure. 7. SEM images of g-C_3N_4 (a), sepiolite (b), g-C_3N_4/Ag_3PO_4@Sep (c) and g-C_3N_4/Fe_3O_4/Ag_3PO_4@Sep (d).

EDX and mapping analyzes

The energy dispersive X-ray spectra (EDX) and the mapping are two of the effective methods for determining the sample chemical composition and its purity. The EDX spectra and image mapping of the synthesized samples, g-C_3N_4, sepiolite, Ag_3PO_4@Sep and g-C_3N_4/Fe_3O_4/Ag_3PO_4@Sep nanocomposite are displayed in **Figure. 8a-d**. The spectrum for the g-C_3N_4 shows, as expected, the presence of C and N elements. Similarly, the raw sepiolite EDX spectrum shown in **Figure. 8b**, indicates the presence in the sample of the O, Mg and Si elements. Moreover, the EDX spectrum of g-C_3N_4/Ag_3PO_4@Sep nanocomposite shows that all the elements in the nanocomposite are found to be matched such as O, Mg, Si, C, N, Ag and P. The EDX spectrum of g-C_3N_4/Fe_3O_4/Ag_3PO_4@Sep nanocomposite indicates the appearance of O, Mg, Si, C, N, Ag, P and Fe elements, and the mapping shows that the g-

C_3N_4, Ag_3PO_4, and Fe_3O_4 elements, are homogeneously distributed on the sepiolite surface. **Table 1** is presented the atomic percentages of different elements.

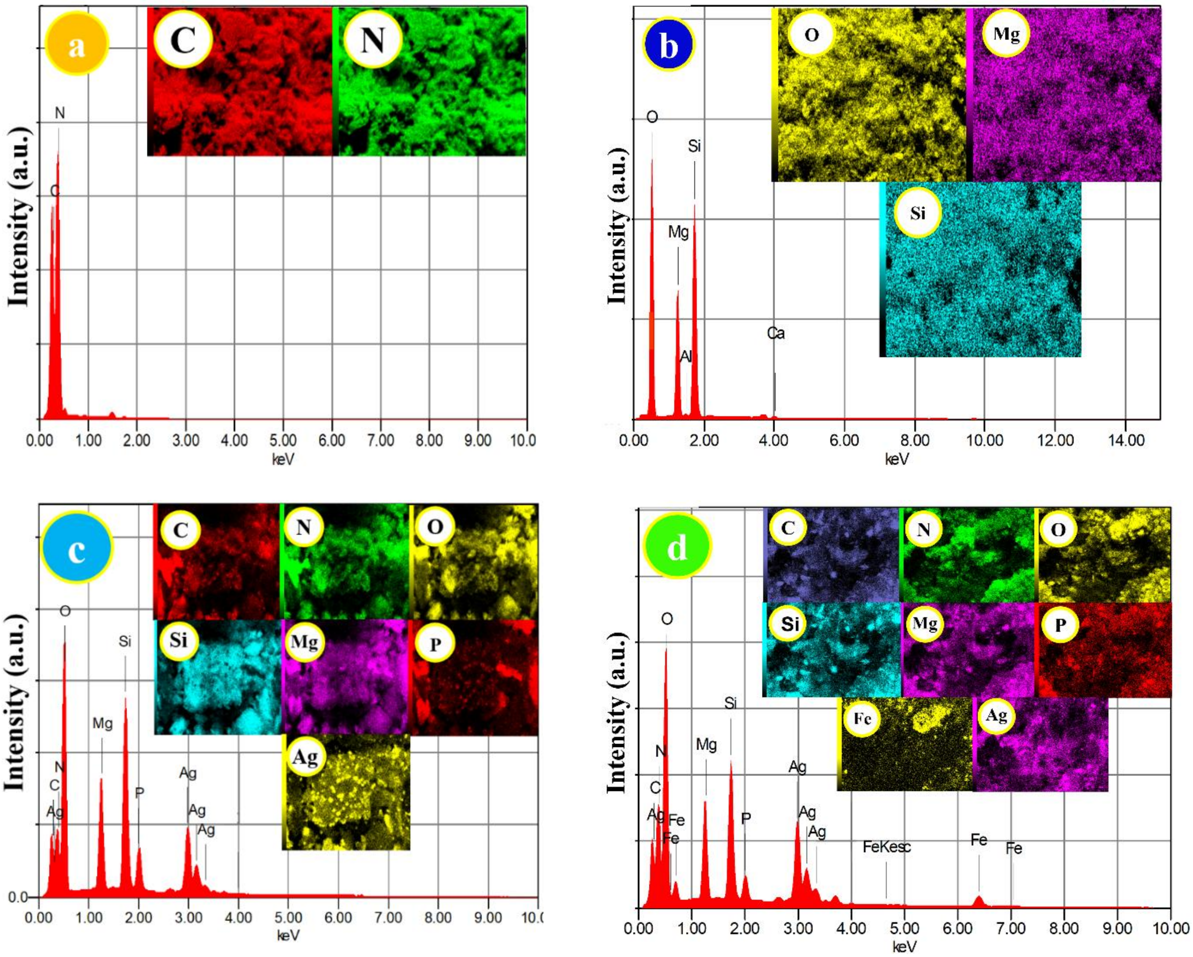

Figure.8. EDX spectra and mapping micrographs, of g-C_3N_4(a), sepiolite (b), g-C_3N_4/Ag_3PO_4@Sep (c) and g-C_3N_4/Fe_3O_4/Ag_3PO_4@Sep (d).

TEM analyzes

Transmission electron microscopy (TEM) is an excellent analytical method in the physical, chemical, sciences can be used to find the morphology and size of different materials. In this study, TEM analysis was used to investigate the particle size and morphology of g-C_3N_4, g-C_3N_4/sepiolite, g-C_3N_4/Ag_3PO_4 and g-C_3N_4/Fe_3O_4/Ag_3PO_4@Sep nanocomposites in details. As shown in **Figure. 9a,** the pristine g-C_3N_4 have uniform fabric-like folded nanosheets fabric-like folded nanosheets with thin thickness porous. The porous structure was favorable for the catalyst to absorb pollutants and further promote the degradation and was in the size range of about 50-80 nm.

Table 1. Atomic percentages of the g-C_3N_4, sepiolite, g-C_3N_4/Ag_3PO_4@Sep and the g- g-C_3N_4/Fe_3O_4/Ag_3PO_4@Sep elements.

		C	**N**	**O**	**Mg**	**Si**	**Ag**	**P**	**Fe**	**Ca**	**Al**
g-C_3N_4	At %	44.59	55.41	-	-	-	-	-		-	-
Sepiolite	At %	-	-	63.56	20.25	15.56	-	-	-	0.43	0.2
g-C_3N_4/Ag_3PO_4@Sep	At %	8.82	4.33	45.35	8.29	21.06	10.13	2.02	-	-	-
C_3N_4/Fe_3O_4/Ag_3PO_4@Sep	At %	9.42	12.02	41.01	7.83	19.04	6.35	2.22	2.1	-	-

The corresponding TEM image of g-C_3N_4/sepiolite is given in **Figure. 9b**. It reveals that the sepiolite shows nanotubes-like fibers having uniform diameters with an average of ~ 30 nm, which exhibited the strong contact between nanosheets g-C_3N_4. The **Figure. 9c** is clearly displayed the strong interfacial contact between g-C_3N_4 and Ag_3PO_4, which is conducive to the rapid transfer and separation of photogenerated electron–hole pairs in g-C_3N_4/ Ag_3PO_4 nanocomposite. Moreover, the Ag_3PO_4 exhibited hexagonal form with a size of ~ 200 nm. In addition, it could be observed from the **Figure. 9d** that all as prepared catalysts nanoparticles g-C_3N_4, Ag_3PO_4 and Fe_3O_4were homogeneously loaded on the nanotubes sepiolite surface. Even more important, the photocatalysts g-C_3N_4 and Ag_3PO_4 are implying the strong interfacial contact between them by Fe_3O_4 nanoparticles, which may favor the charge transfer. So, the obtained results reinforce what was previously obtained by several analysis techniques.

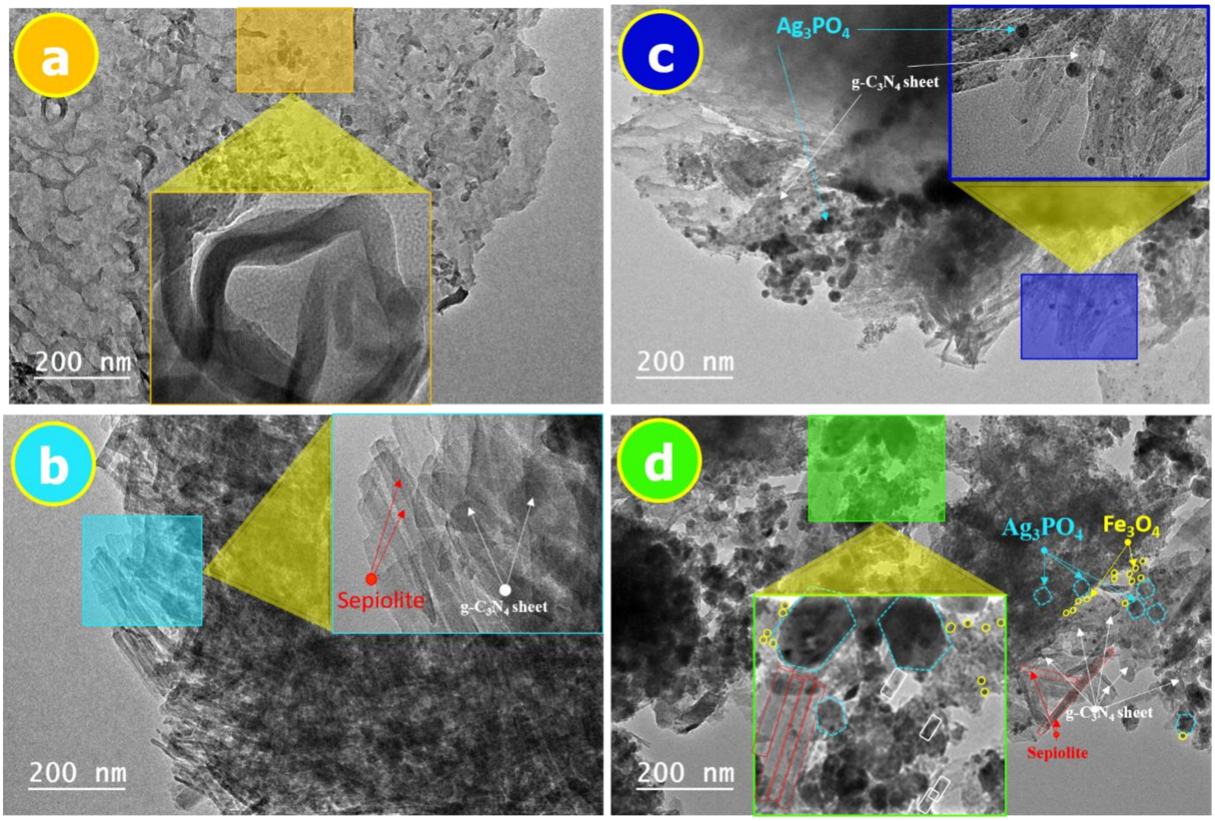

Figure. 9. TEM images of the g-C_3N_4 (a), g-C_3N_4/sepiolite (b), g-C_3N_4/Ag_3PO_4 (d) and C_3N_4/Fe_3O_4/Ag_3PO_4@Sep

XPS analyzes

XPS is commonly quantitative technique used to provide information on the elemental composition and the valance states of constituent elements on the surface of the nanomaterials. Nevertheless, the chemical species in the surface of g-C_3N_4, g-C_3N_4/sepiolite, -C_3N_4/Ag_3PO_4 / Sep and g-C_3N_4/Fe_3O_4/Ag_3PO_4@Sep nanocomposites were confirmed by XPS and reported in **Figure.10**. The XPS spectrum of g-C_3N_4 **10a** reveals mainly two peaks assigned to C1s and N1s, the spectrum of g-C_3N_4/sepiolite **Figure. 10a** shows seven main elements C 1s, N 1s, Si 2p, O 1s, Mg 2p, O Auger and Mg Auger. Moreover, the spectrum of g-C_3N_4/Ag_3PO_4 (**Figure. 10a**) includes all peaks of g-C_3N_4 and sepiolite as well as four elements P2p, Ag $3d_{3/2}$, Ag $3d_{5/2}$and Ag3p.The XPS spectrum of g-C_3N_4/Fe_3O_4/Ag_3PO_4@Sep nanocomposite is reported in **Figure. 10a,** it can be seen that all peaks of g-C_3N_4, sepiolite and Ag_3PO_4 are existing as well as element Fe 2p, which confirm the presence of Fe_3O_4 in the surface of sepiolite.**Figure.10b** shows the high-resolution XPS spectra of the peak of Si 2p located in the region of 101.97 eV, which revealing the valence state of the silicon.

Figure.10c detects the deconvoluted Mg 2s spectra located at 1303.2 eV, which can be attributed to magnesium hydroxides Mg-OH. In **Figure. 10d**, the C 1s spectrum can be decomposed into two constituents at 284.8 and 288.3 eV for the C-C and C-N chemical bonding, respectively[30, 31].The N 1s peak of g-C_3N_4 could be deconvoluted into three Gaussian−Lorentzian fitted peaks at 398.96, 399.67, and 400.9 eV, which were attributed to pyridinic N (C-N=C), pyrrolic N (N-$(C)_3$, and graphitic N (C-N-H) respectively (**Figure. 10e**)[32, 33].The deconvoluted Ag3d spectra demonstrate the existence of two main peaks at 367.2 and 373.17 eV (**Figure. 10f**), assigned to the Ag3$d_{5/2}$ and Ag3$d_{3/2}$ of Ag^+ in the nanocomposite. The deconvolution of O1s from the nanocomposite display two principal peaks at 531.1 and 532.32 eV, corresponding to and the lattice oxygen atoms (O^{2-}) and H_2O molecules adsorbing on the surface of nanocomposite **Figure. 10g** [34, 35]. Deconvolution Fe 2p orbital presents two main spectrum located at 711.97 and 725.56 eV, could be due to the Fe 2p $_{3/2}$ and Fe 2p $_{1/2}$ spin orbitals of magnetite, respectively, **Figure. 10h** [36].As can be seen in **Figure 10.i**. the peak at 132.8eV may be attributed to the P2p, which is assigned to P^{5+} of PO_4^{3-}[36]. Therefore, these results could confirm the coexistence of g-C_3N_4, Ag_3PO_4 and Fe_3O_4 in the g-C_3N_4/Fe_3O_4/Ag_3PO_4@Sep nanocomposites, and then create an important synergistic effect during the photocatalytic activity.

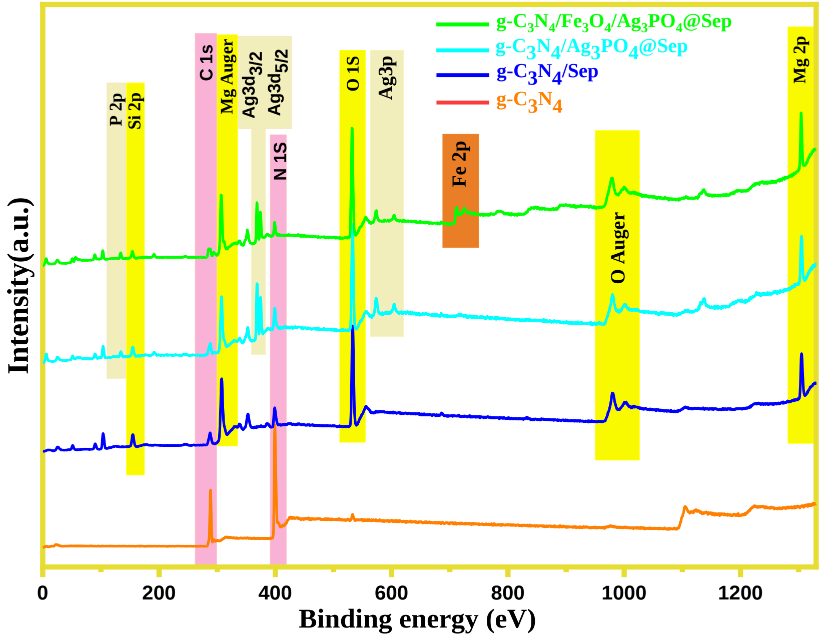

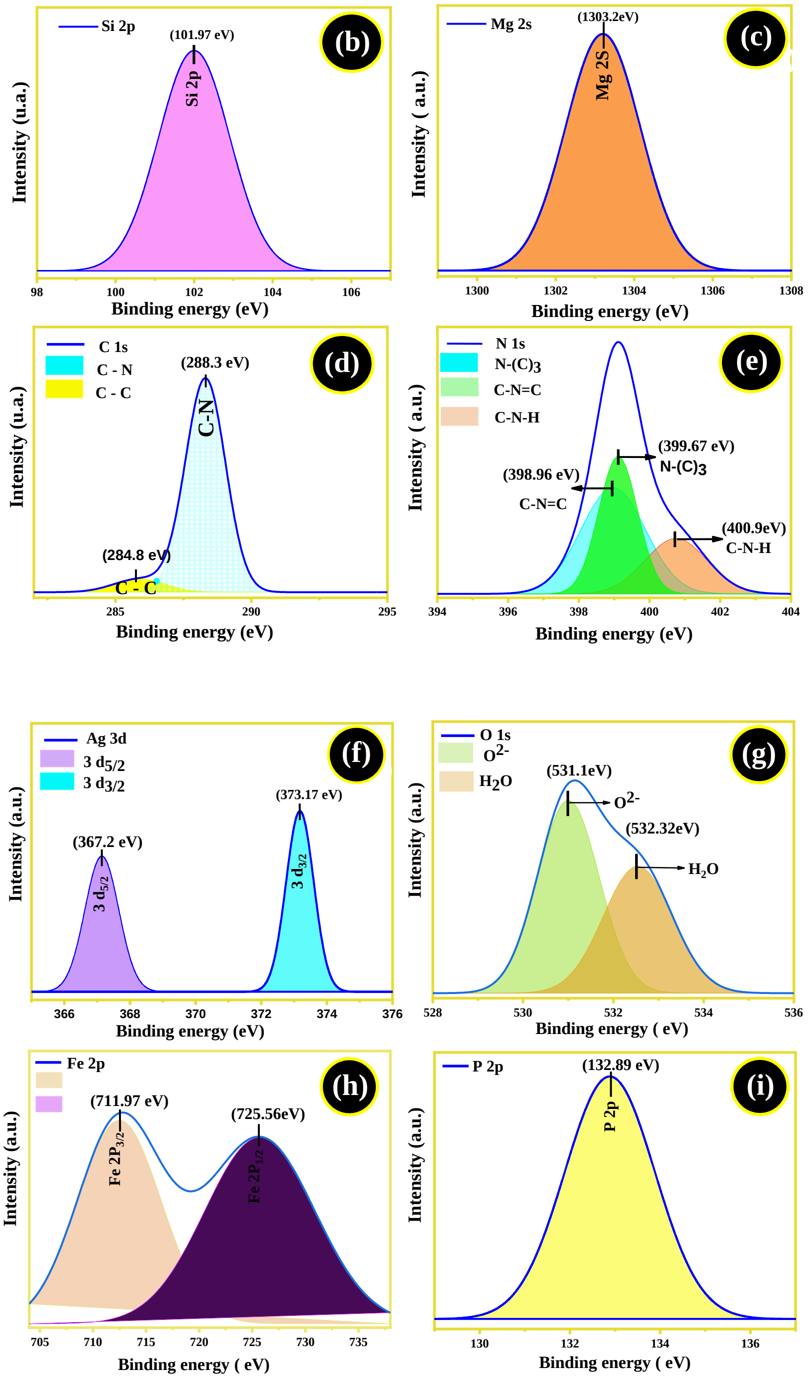

Figure. 10. XPS analyzes of g-C_3N_4, g-C_3N_4/Sep, g-C_3N_4/Ag_3PO_4@Sep and g-C_3N_4/Fe_3O_4/Ag_3PO_4@Sep nanocomposite (a) HR Si 2p spectrum (b) HR Mg 2s and (c) HR C 1s (d)HR N1s (e) HR Ag 3d (f)HR O1s (g) HR Fe 2p (h) HR P 2p (i).

DRS analyzes

Solid-state UV-Vis or diffuse reflectance spectroscopy (DRS) is a very useful technique to investigate the electronic and optical properties of catalysts samples. It can be observed from

Figure.11a that all samples exhibited good light capture in the range of 200 to 500 nm, the DRS spectrum shows an absorption band edge at □ 440 nm corresponding to intrinsic absorption of g-C_3N_4 and Ag_3PO_4 demonstrated an absorption band edge at □450 nm. When Ag_3PO_4, g-C_3N_4 and Fe_3O_4 were supported on sepiolite, the optical absorption range was broader, and the optical absorption intensity over the whole range of 200 -600 nm. This indicates that Ag_3PO_4, g-C_3N_4, Fe_3O_4 and sepiolite have a synergistic effect. Thus, the increase in the absorption of g-C_3N_4/Fe_3O_4/Ag_3PO_4@Sep nanocomposite indicates that the nanocomposite may demonstrate a remarkable photocatalytic activity in the visible region.

The band gaps of three samples can be calculated according to the Kubelka-Munk formula, which is the following (**Eq.2**)[37, 38]:

$$\alpha h\nu = A(h\nu - Eg)^{n/2} \qquad (2)$$

Where α is the absorption coefficient, h is Planck's constant, ν is the frequency of light, Eg represents the band gap energy, A is a constant and n refers to the type of electron transition.**Figure. 11b** shows $(\alpha h\nu)^2$ versus energy (hν) diagrams of the band gap energy of g-C_3N_4, Ag_3PO_4 and g-C_3N_4/Fe_3O_4/Ag_3PO_4@Sep. As illustrated by the Tauc plot in **Figure. 11b** the band gap energies of g-C_3N_4, Ag_3PO_4 and g-C_3N_4/Fe_3O_4/Ag_3PO_4@Sep are 2.94, 2.44 and 2.83 eV, respectively. So, the narrow band gap of the g-C_3N_4/Fe_3O_4/Ag_3PO_4@Sep nanocomposite due to the existence of synergistic effect between sepiolite, Ag_3PO_4, g-C_3N_4 and Fe_3O_4 shows that it has a higher visible light absorption ability, which could help in the separation of electron-hole pairs.

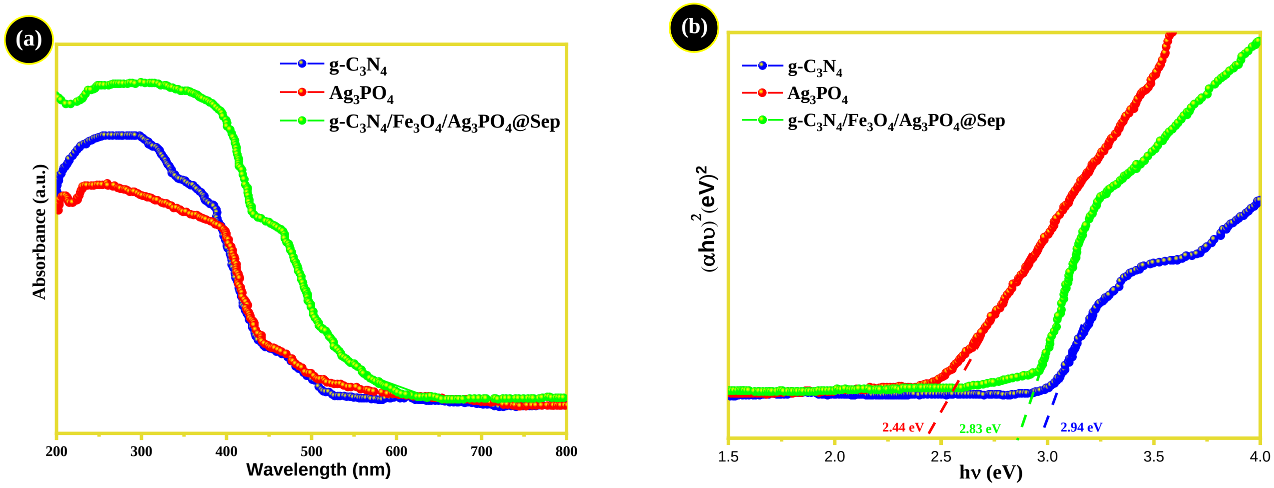

Figure. 11. (a) UV–Vis diffuse reflectance spectra and (b)Tauc plot of the prepared samples: g-C_3N_4, Ag_3PO_4 and g-C_3N_4/Fe_3O_4/Ag_3PO_4@Sep.

3.2. Photocatalytic activity of g-$C_3N_4/Fe_3O_4/Ag_3PO_4$@Sep nanocomposite

The photocatalytic activities of all synthesized photocatalysts were examined by degradation of MG dye under sunlight irradiation to study their potential applicability in the field of environmental treatment.

Firstly, the photodegradation of MG without catalyst was studied for comparison (i. e. MG aqueous solution irradiated with sunlight in the absence of the photocatalyst). In the absence of the photocatalyst (**Figure. 12a**), the results indicate that no degradation of MG was observed after 12 minutes of irradiation. This indicated that MG dye is not effectively decontaminated by photolysis alone (i.e. under sunlight irradiation and in the absence of the photocatalyst). In the other hand, as can be seen in **Figure. 12a**, in the absence of Sunlight irradiation, the adsorption of MG from water onto the prepared catalyst surfaces, such as, g-C_3N_4, g-C_3N_4/Sep, g-C_3N_4/Ag_3PO_4@Sep and g-$C_3N_4/Fe_3O_4/Ag_3PO_4$@Sep nanocomposites, were also investigated. It can be seen from **Figure. 12a** that the MG dye molecules were only slightly removed from water after 60 minutes. The removal efficiencies of the MG dye, in the absence of Sunlight irradiation, achieved approximately 13%, 10%, 7% and 2% for g-C_3N_4, g-C_3N_4/Ag_3PO_4@Sep, g-C_3N_4/Sep and g-$C_3N_4/Fe_3O_4/Ag_3PO_4$@Sep nanocomposite, respectively. These data indicate that all the synthesized photocatalysts show low adsorption activities towards the MG dye.

Besides**, Figure. 12b** shows the MG dye removal, under Sunlight irradiation, from aqueous media onto different types of prepared photocatalysts, including g-C_3N_4, g-C_3N_4/Sep, g-C_3N_4/Ag_3PO_4@Sep and g-$C_3N_4/Fe_3O_4/Ag_3PO_4$@Sep nanocomposite during the same period. The observed degradation efficiencies for MG dye are about ≈ 23.91%, ≈25.52%, ≈76.55% and ≈100%, for the g-C_3N_4, g-C_3N_4/Sep, g-C_3N_4/Ag_3PO_4@Sep and g-$C_3N_4/Fe_3O_4/Ag_3PO_4$@Sep nanocomposite in the 12 min of irradiation, respectively. Obviously, the order of photocatalytic activity of the prepared photocatalysts is: g-$C_3N_4/Fe_3O_4/Ag_3PO_4$@Sep > g-C_3N_4/Ag_3PO_4@Sep > g-C_3N_4/Sep >g-C_3N_4. **Figure. 12b** shows clearly that the concentration of MG dye decreases dramatically, as time increases, and nearly disappears within only 16 min. So, the results obtained demonstrate that the photocatalytic activity of g-$C_3N_4/Fe_3O_4/Ag_3PO_4$@Sep nanocomposite towards MG dye, under sunlight irradiation, is higher in comparison to the others photocatalysts. Such difference in behaviour between g-$C_3N_4/Fe_3O_4/Ag_3PO_4$@Sep and the others catalysts, can be due to several effects. Firstly, the magnetic nanocomposite exhibits high ability to absorb visible light. Secondly, the synergistic effect occurring between the three samples: Ag_3PO_4, g-C_3N_4 and Fe_3O_4, leading to photoactivity enhancement. Thirdly, the high electrostatic interactions occurring between the Ag_3PO_4 nanoparticles and the sepiolite negative sites, lead to the stability of Ag_3PO_4 nanoparticles caused by the strong adhesion of Ag_3PO_4 on the sepiolite surface, improve the electrons and holes separation, and prevent their recombination. Fourthly, the increase in the degradation efficiency is due to the availability of more active sites in the g-C_3N_4/Fe_3O_4/Ag_3PO_4@Sep nanocomposite. Fifthly, the sepiolite was used as an excellent support by increasing the contact between Ag_3PO_4 and the solar-light photons. Finally, the Fe_3O_4 nanoparticles can be used as an efficient electron transfer compound leading to recombination reduction of the photogenerated carriers and facilitating the transfer of photogenerated electrons. Therefore, it can be concluded that the preparation of the magnetic Z-heterojunction g-C_3N_4/Fe_3O_4/Ag_3PO_4@Sep should be used as a stronger photocatalyst for the degradation of hazardous organic pollutants such as toxic dyes. Furthermore, the photocatalytic performance of the magnetic nanocomposite prepared in the present work, was evaluated and compared with other photocatalysts found in the literature (**Table 2**). Besides, the experimental kinetic data for the MG dye photodegradation in the presence of the g-C_3N_4/Fe_3O_4/Ag_3PO_4@Sep nanocomposite were assessed and compared to the first-order Langmuir-Hinshelwood model. Thus, according to (**Eq. 3**) the apparent degradation rate constant of the first-order reaction, $\mathbf{K_{app}}$, can be calculated from the plot of ln (C_0/C_t) versus t. Knowing the K_{app} value, the half-life $\mathbf{t_{1/2}}$ value can also be determined according to (**Eq.** 4):

$$\ln\left(\frac{C_0}{C_t}\right) = K_{app} \times t \tag{3}$$

$$t_{1/2} = \frac{0.693}{K_{app}} \tag{4}$$

where K_{app} (min^{-1}) is the apparent degradation rate constant of the first-order reaction, t is the irradiation time (min), C_o (mg/L) and C_t (mg/L) are the initial and residual concentrations of MG dye.

The linearization of ln (C_t/C_0) as a function of irradiation time for each photocatalyst is given in **Figure. 12c**. The calculated values of K_{app} and half-life $t_{1/2}$ were also reported in **Table 3**.

Table 2. Comparison of photocatalytic activity of g-C_3N_4/Fe_3O_4/Ag_3PO_4@Sep towards MG dye with other similar photocatalysts from literature.

Photocatalyst	Light Source	C_0 (mg/L)	Time (min)	%	Ref
ZnO/CNT	Visible light	30	60	79 %	[39]
α-$NiMoO_4$	UV– Visible	10	180	79.43 %	[40]
poly(azomethine)/TiO_2	Sunlight	50	300	95	[41]
rGO/CuS	Sunlight	10	90	97.6%	[42]
Fe_3O_4/ SiO_2/TiO_2	UV	10	150	100%	[43]
Pt-TiO_2/SiO_2	UV–Vis. light	10	60	79%	[44]
RGO-Fe_3O_4/TiO_2	UV–Visible	5.5	55	100	[45]
g-C_3N_4/Fe_3O_4/Ag_3PO_4@Sep	**Sunlight**	**10**	**12**	**100**	**This work**

Table 3. MG dye degradation parameters for different prepared photocatalysts.

	g-C_3N_4	g-C_3N_4@Sep	g-C_3N_4/Ag_3PO_4@Sep	g-C_3N_4/Fe_3O_4/Ag_3PO_4@Sep
K_{app} (min^{-1})	0.0097	0.01	0.143	0.264
$t_{1/2}$ (min)	4.34	4.238	1.64	0.96

The obtained rate constants (K_{app}) values for the g-C_3N_4, g-C_3N_4@Sep, g-C_3N_4/Ag_3PO_4@Sep and g-C_3N_4/Fe_3O_4/Ag_3PO_4@Sep nanocomposites are, 0.0097, 0.01, 0.143 and 0.26 min^{-1}, respectively. The use of the g-C_3N_4/Fe_3O_4/Ag_3PO_4@Sep nanocomposite indicates enhancement of the MG dye photocatalytic degradation, under solar irradiation, leading to a higher rate constant K_{app} value, which is □27, 26 and 1.85 times higher than g-C_3N_4, g-C_3N_4@Sep, g-C_3N_4/Ag_3PO_4@Sep, respectively. Therefore, the photocatalytic enhancement of magnetic nanocomposite g-C_3N_4/Fe_3O_4/Ag_3PO_4@Sep to degrade organic molecules such as MG dye under solar light irradiation was attributed to the synergy effects occurring between Ag_3PO_4 supported by sepiolite clay and g-C_3N_4 combined with the Fe_3O_4 nanoparticles.

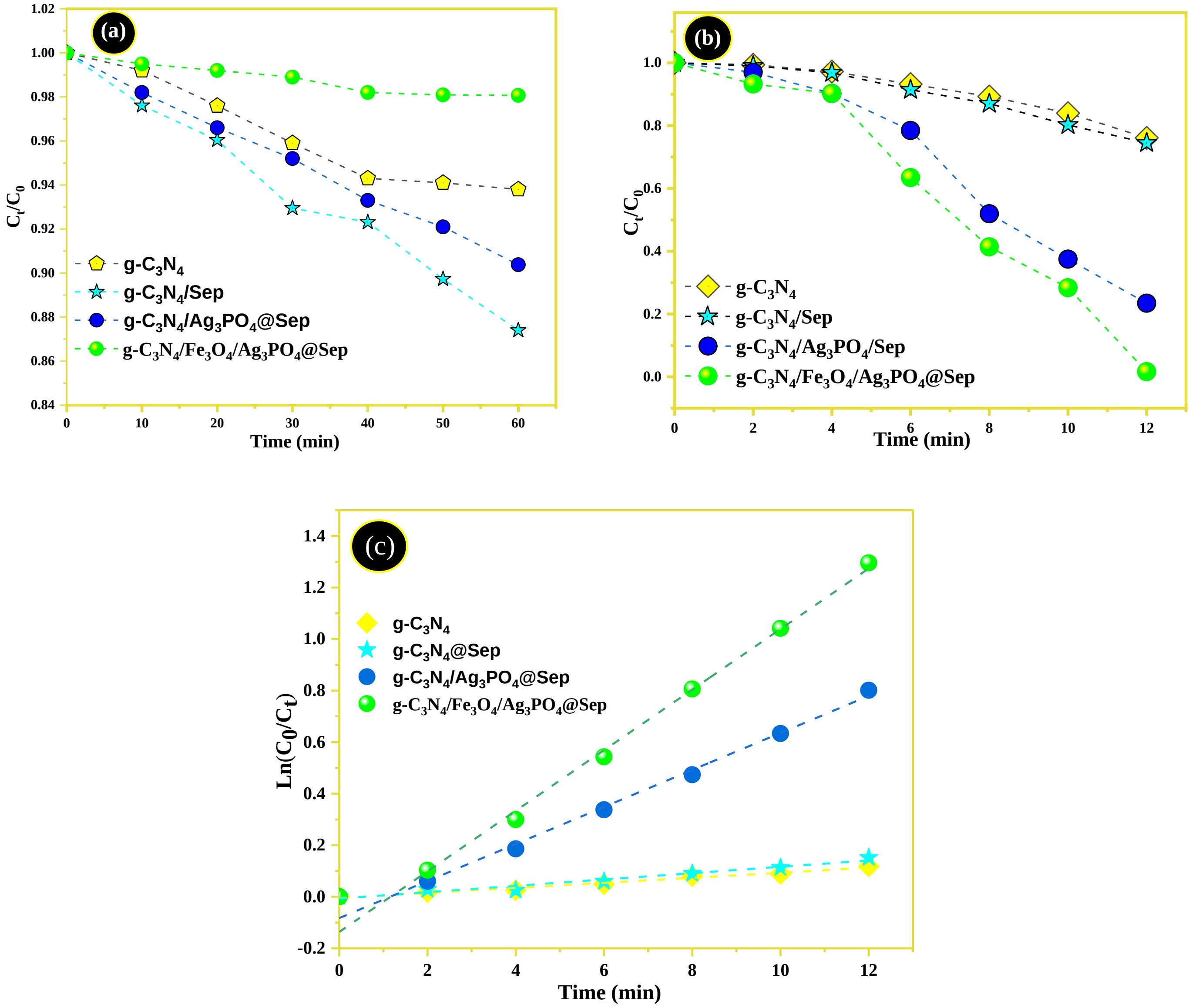

Figure.12. Irradiation of MG aqueous solution in the absence of the photocatalyst, and adsorption curves of MG dye from water onto various prepared samples, in the absence of the sunlight irradiation (a). Photocatalytic activities in the presence of various photocatalysts for MG degradation, and under sun light irradiation (b). Pseudo-first-order kinetic plot for degradation of the MG dye (c).

The pH is one of the important factors in the photocatalytic process because it affects the surface charge of the photocatalyst, degree of ionization of the target organic pollutants and dissociation of the functional groups on the active site of the photocatalyst [46]. **Figure.13** displays the influence of initial pH on the photodegradation of malachite green (10 mg. L^{-1}) catalyzed by g-$C_3N_4/Fe_3O_4/Ag_3PO_4$@Sep, which were performed by changing the pH in the range of 3-11 and adjusted by NaOH (0.1 M) or HCl (0.1 M). It is observed that the g-$C_3N_4/Fe_3O_4/Ag_3PO_4$@Sep nanocomposite exhibits the greatest photocatalytic efficiency at pH = 7 (approximately 100%). However, in the acidic medium is reduced to 65.76% and 83.53% at pH = 3 and pH=5 which can be due to the fact that in acidic media, the surface of Sepiolite can be surrounded by the positive charges of H^+, which prevents the cationic MG molecules from reaching the active site active site of Ag_3PO_4 and g-C_3N_4. Nevertheless, under a strongly alkaline solution pH =9 and pH =11, the degradation efficiency is decreased to 25.15% and 20.62%. This can be related to the instability of g-$C_3N_4/Fe_3O_4/Ag_3PO_4$@Sep nanocomposite in a strong alkaline solution (Ag_3PO_4 can react with NaOH to form Ag_2O, and then reduces the degradation performance). Hence, pH=7 was found to be more adequate for MG degradation.

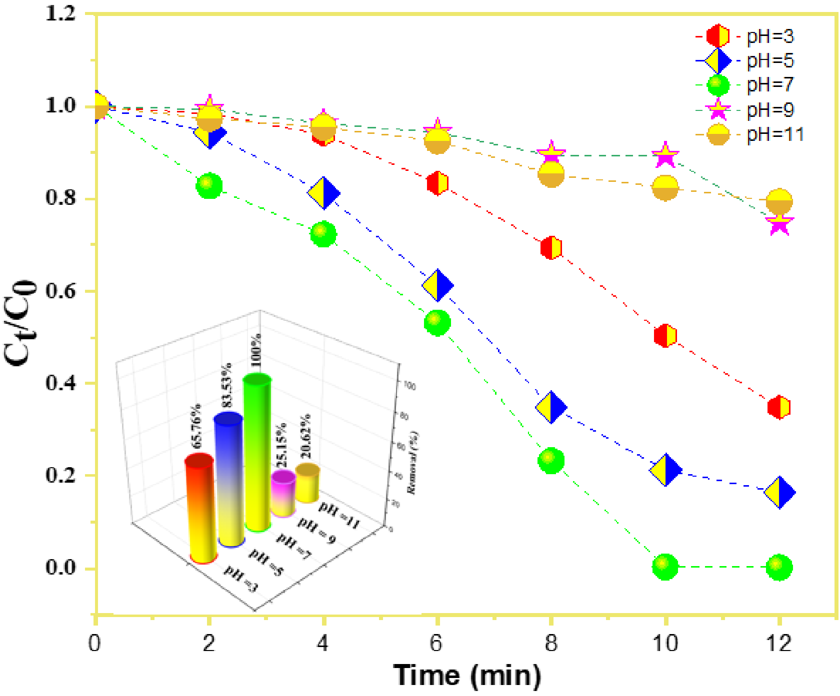

Figure. 13 Effect of pH values on MG photocatalytic degradation by g-$C_3N_4/Fe_3O_4/Ag_3PO_4$@Sep

3.3. Possible photocatalytic mechanism

In order further to understand the photocatalytic mechanism of g-$C_3N_4/Fe_3O_4/Ag_3PO_4$@Sep nanocomposites in details. Several active species, like the hydroxyl radical (${}^{\bullet}OH$), the hole (h^+), and the superoxide anion radical (${}^{\bullet}O_2^-$) are participate in the photodegradation processes, and the function of active species generated by nanocomposite photocatalysts is evaluated with different scavengers. However, the typical radical trapping tests for MG dye degradation were examined in the presence of ethylenediamine tetra-acetic acid disodium (EDTA-2Na), L-ascorbic acid (ASC), and Isopropanol Alcohol (IPA), which are utilized as capture agents for h^+, ${}^{\bullet}O_2^-$, and ${}^{\bullet}OH$, respectively [37]. It can be seen from **Figure. 14** that the removal rate of MG by g-$C_3N_4/Fe_3O_4/Ag_3PO_4$@Sep photocatalyst was achieved up to 100 % under 12 minutes of visible light irradiation, without the introduction of a capture agent. Besides, the decolorization activity of g-$C_3N_4/Fe_3O_4/Ag_3PO_4$@Sep nanocomposite towards MG dye in the presence of EDTA-2Na, IPA and ASC decreased to 16.35%, 10.44% and 87.6%, respectively, indicating that ${}^{\bullet}O_2^-$ was not the main reactive species in the degradation photocatalytic activity. Whereas the photocatalytic activity was strongly inhibited by the introduction of EDTA- 2Na and IPA, which indicated that that h^+ and ${}^{\bullet}OH$ are the major reactive species in the photocatalytic degradation of MG. Therefore, h^+ and ${}^{\bullet}OH$ radical are expected to be the main reactive species for g-$C_3N_4/Fe_3O_4/Ag_3PO_4$@Sep nanocomposite in the photocatalytic degradation process of MG under sunlight illumination. While (${}^{\bullet}O_2^-$) played a secondary role. The same results were obtained in the previous study [13].

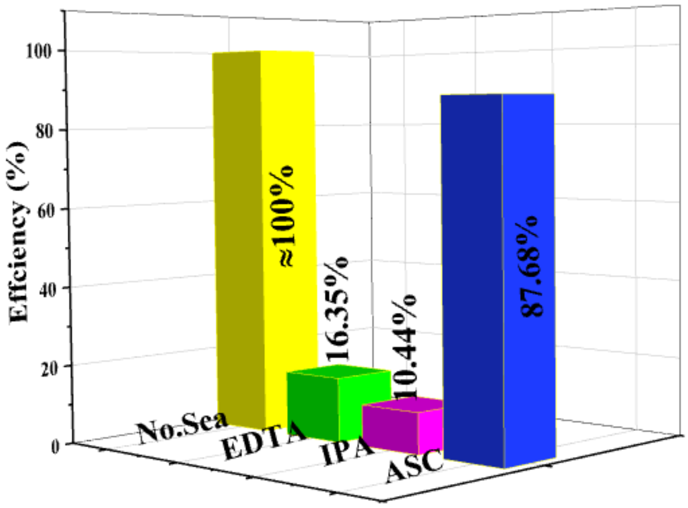

Figure. 14. Effect of scavengers on the photocatalytic degradation of MG by g-$C_3N_4/Fe_3O_4/Ag_3PO_4$@Sep nanocomposite.

The possible mechanism of the improved photocatalytic activity for g-$C_3N_4/Fe_3O_4/Ag_3PO_4$@Sep toward MG dye was investigated based on our previous experimental and schematically illustrated in **Figure. 15**. For two pure Ag_3PO_4 and g-C_3N_4, the electrons and holes photogenerated tend to recombine, and then only a proportion of them participated in the photocatalytic reaction. Thus, resulting in a comparatively low photocatalytic activity. However, the CB and VB positions of Ag_3PO_4 and g-C_3N_4 were determined using the empirical equations as shown below[46]:

$$\chi(A_aB_bC_c) = [\chi(\mathrm{A})^a.\chi(\mathrm{B})^b.\chi(\mathrm{C})^c]^{\frac{1}{a+b+c}} \quad \textbf{(5)}$$

$$E_{CB} = \chi - E_0 - \frac{E_g}{2} \quad \textbf{(6)}$$

$$E_{VB} = E_{CB} + E_g \quad \textbf{(7)}$$

where χ indicates the absolute electronegativity of the semiconductor,which is defined as the geometric mean of the absolute electronegativity of the constituent atoms, E_0 is the energy of free electrons on the hydrogen scale (about 4.5 eV vs. NHE) and Eg (eV) the band gap energy of the semiconductors. The χ values for Ag_3PO_4 and g-C_3N_4 are calculated to be 5.96 and 4.73, respectively. The CB and VB positions of g-C_3N_4 are determined to be-1.24 and +1.7 eV, respectively, whereas those of Ag_3PO_4 are about +0.13 and +2.68 V, respectively (**Table 4**). In this study the sepiolite clay was used as a support for the three semiconductors which helped to increase the adsorptive properties of the g-$C_3N_4/Fe_3O_4/Ag_3PO_4$@Sep nanocomposite surface, and to enhance its anionic active sites density, leading to removal from water of more hazardous MG dye molecules [43].

Due to the irradiation of sunlight, the electrons in the valence band (VB) of Ag_3PO_4 can be rapidly transferred from the conduction band (CB) leaving holes (h^+). Besides, the g-C_3N_4 was also very activated by sunlight photons, and the generate the electrons in the counduction band (CB) and holes in the valance band (VB). At the same time, the Fe_3O_4 nanoparticles were used as a solid electron mediator to link Ag_3PO_4 and g-C_3N_4 and can it enhances the electron transfer capability of photocarriers. On the other hand, the photo-generated electrons (e^-) formed in the CB of Ag_3PO_4 were captured by the Fe_3O_4 nanopartcules and transferd rapidly to VB of g-C_3N_4, because the $^{\bullet-}O_2$ radicals cannot be formed in the surface of Ag_3PO_4 due to the CB potential (E_{CB} = 0.24 eV) is more positive than that of the $O_2/^{\bullet-}O_2$ potential (−0.046 V vs NHE)[47].Neverthless, g-C_3N_4 can react with O_2 to produce the $OH^\bullet$ radical species through the reduction of O_2 to H_2O_2, followed by the further reduction of H_2O_2 to OH^- and the $OH^\bullet$ radical species. This is due to the CB edge potential of g-C_3N_4 (E_{CB} = - 1.24 eV / NHE) being more lower than the standard potential of the O_2/H_2O_2 redox couple, which is 0.68 eV at the normal hydrogen electrode (NHE). Consequently, the accumulation of electrons in the CB of g-C_3N_4 and the holes in the VB of Ag_3PO_4 exhibited a high reduction and oxidation ability to mineralize MG dyes in H_2O and CO_2, respectively. In the above results, it is clear that the fabricated nanocomposite act as a Z-scheme photocatalysts and the synergistic effect between three synthesizied semiconductor play a curcial role in the enhanced photoctalytic efficiency. Consequently, the photodegradation activity of g-$C_3N_4/Fe_3O_4/Ag_3PO_4$@Sep toward MG dye could be displayed as follows:

$$\mathbf{Ag_3PO_4 + h\upsilon \rightarrow Ag_3PO_4\ (e_{CB}^{-} + h_{VB}^{+})} \quad \mathbf{(8)}$$

$$\mathbf{g\text{-}C_3N_4(e^{-}) + h\upsilon \rightarrow g\text{-}C_3N_4\ (e_{CB}{-}{+}h_{VB}^{+})} \quad \mathbf{(9)}$$

$$\mathbf{O_2 + 2H^{+} + g\text{-}C_3N_4\ (2e^{-}) \rightarrow H_2O_2 + g\text{-}C_3N_4} \quad \mathbf{(10)}$$

$$\mathbf{H_2O_2 + g\text{-}C_3N_4\ (e^{-}) \rightarrow OH^{-} + {}^{\bullet}OH + g\text{-}C_3N_4} \quad \mathbf{(11)}$$

$$\mathbf{Ag_3PO_4\ (h^{+}) + Malachite\ Green\ dye \rightarrow H_2O + CO_2 + simple\ molecules} \quad \mathbf{(12)}$$

$$\mathbf{{}^{\bullet}OH + Malachite\ Green\ dye \rightarrow H_2O + CO_2 + simple\ molecules} \quad \mathbf{(13)}$$

Table 4. Values of the electronegativity (χ), the bang gap energy (Eg), and the potential energy for valence band (E_{VB}) and conduction band (E_{CB}), for the g-C_3N_4 and Ag_3PO_4 catalysts.

catalyst	χ	**Eg (eV)**	**CB (eV)**	**VB (eV)**
g-C_3N_4	4.73	2.94	-1.24	1.7
Ag_3PO_4	5.96	2.44	0,24	2,68

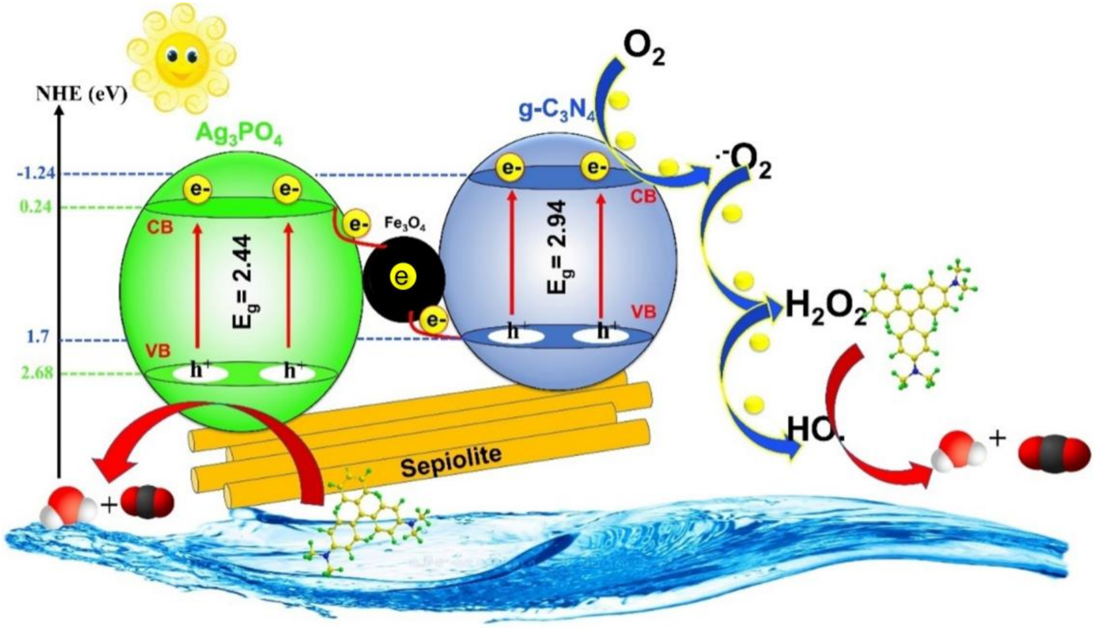

Figure. 15 : Schematic Illustration of Photocatalytic activity toward MG dye using g-$C_3N_4/Fe_3O_4/Ag_3PO_4$@Sep nanocomposite under sun-Light Irradiation.

3.4. Reusability and stability

The stability of photocatalysts is also an essential characteristic from the point of view of practical applications[49]. To investigated stability and the reusability of the g-$C_3N_4/Fe_3O_4/Ag_3PO_4$@Sep and Ag3PO4 samples, the recycle experiments for the degradation of MG dye under sunlight illumination in 12 min was studied. As illustrated in **Figure. 16**, after four cycles, the degradation of MG dye by pure Ag_3PO_4 exhibited an evident decrease (<22%) due to their high solubility in aqueous solution and the photoreduction of Ag^+ in Ag_3PO_4 to metallic Ag under sunlight illumination ($4Ag_3PO_4 + 6H_2O + 12\ h^+ + 12e^- \rightarrow 12Ag + 4H_3PO_4 + 3O_2$). Also, part of the pure Ag_3PO_4 may degrade to Ag_2O when Ag_3PO_4 is used. In the other hand (<13%), the photocatalytic activity of g-$C_3N_4/Fe_3O_4/Ag_3PO_4$@Sep nanocomposite shows a small loss, suggesting that the nanocomposite photocatalyst is comparatively stable during the photocatalytic degradation of MG dyes, which might be due to the fact that g-C_3N_4, Fe_3O_4 and sepiolite prevented Ag_3PO_4 from being reduced to metallic silver under sunlight irradiation. However, the color of the g-$C_3N_4/Fe_3O_4/Ag_3PO_4$@Sep nanocomposite slightly changed, while the pure Ag_3PO_4 changed to gray. We hypothesized that the photocorrosion phenomenon happened in the pure Ag_3PO_4 nanoparticles. Thus, the enhanced photostability of g-$C_3N_4/Fe_3O_4/Ag_3PO_4$@Sep had the potential for long-term wastewater purification.

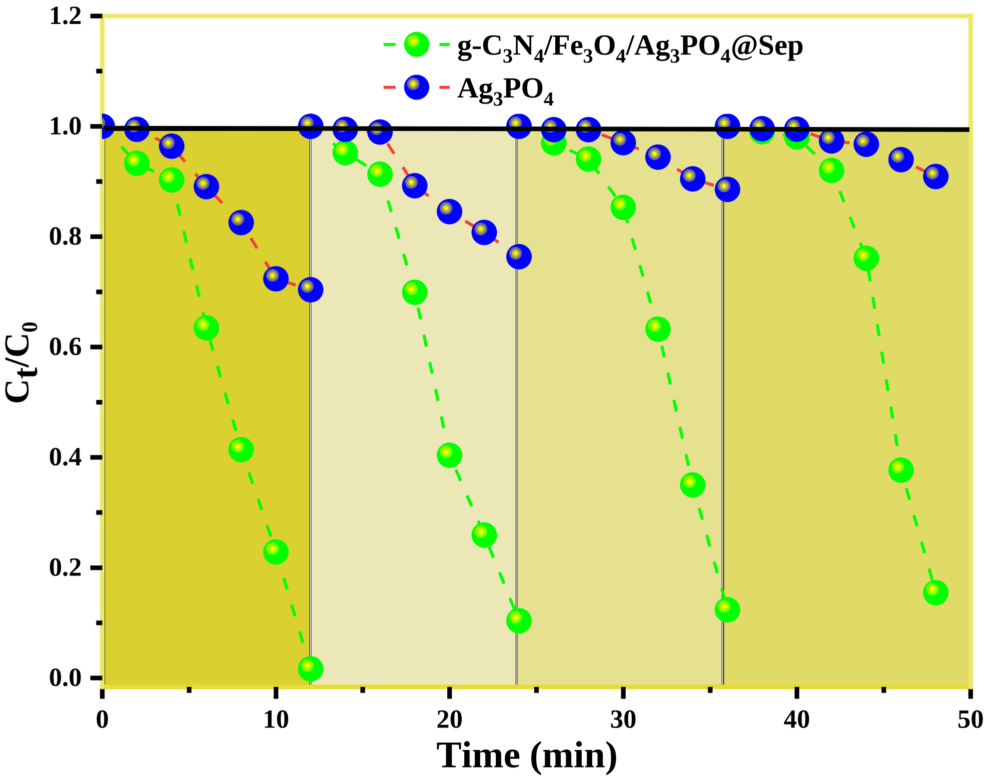

Figure. 16. Cycling runs for photocatalytic degradation of MG dye using g-$C_3N_4/Fe_3O_4/Ag_3PO_4$@Sep and Ag_3PO_4 under sunlight irradiation.

3.5. The formation of nano-composite Fe_3O_4/Ag_3PO_4@Sep by Monte Carlo adsorption locator simulation

After optimization of structures by quantum calculations based on DFT-D, the adsorption performance of 6 of g-C_3N_4, Ag_3PO_4 and Fe_3O_4 molecules on Sep was occurred to make Fe_3O_4/Ag_3PO_4@Sep surface by adsorption locator module and forcefield; universal in Materials Studio 2017 software (ball-and-stick structures of nanocomposite are in **Figures 17a-b**. The total energy of the system after the adsorption of C_3N_4, Ag_3PO_4 and Fe_3O_4 (E_{ad}) on Sep was obtained about -4.984 × 10^3 kcal/mol, resulting in coadsorbed g-C_3N_4, Ag_3PO_4 and Fe_3O_4 owing to the high negative value and exothermic system. In other hand, the calculated adsorption energy of this configuration was the most stable. Additionally, the top view of the Fe_3O_4 molecule vertically adsorbed on Sep are shown in **Figure.2b**. The energy of rigid adsorption, deformation, E_{ads} of Ag_3PO_4, Fe_3O_4 and C_3N_4 was obtained -439.766, -4.544 × 10^3, -11.147, -478.748 and -335.253, respectively. By analysis and comparison, adsorption energy for Fe_3O_4 and g-C_3N_4 parallel to Sep and their adsorption energies of both configurations were higher than that of Ag_3PO_4.

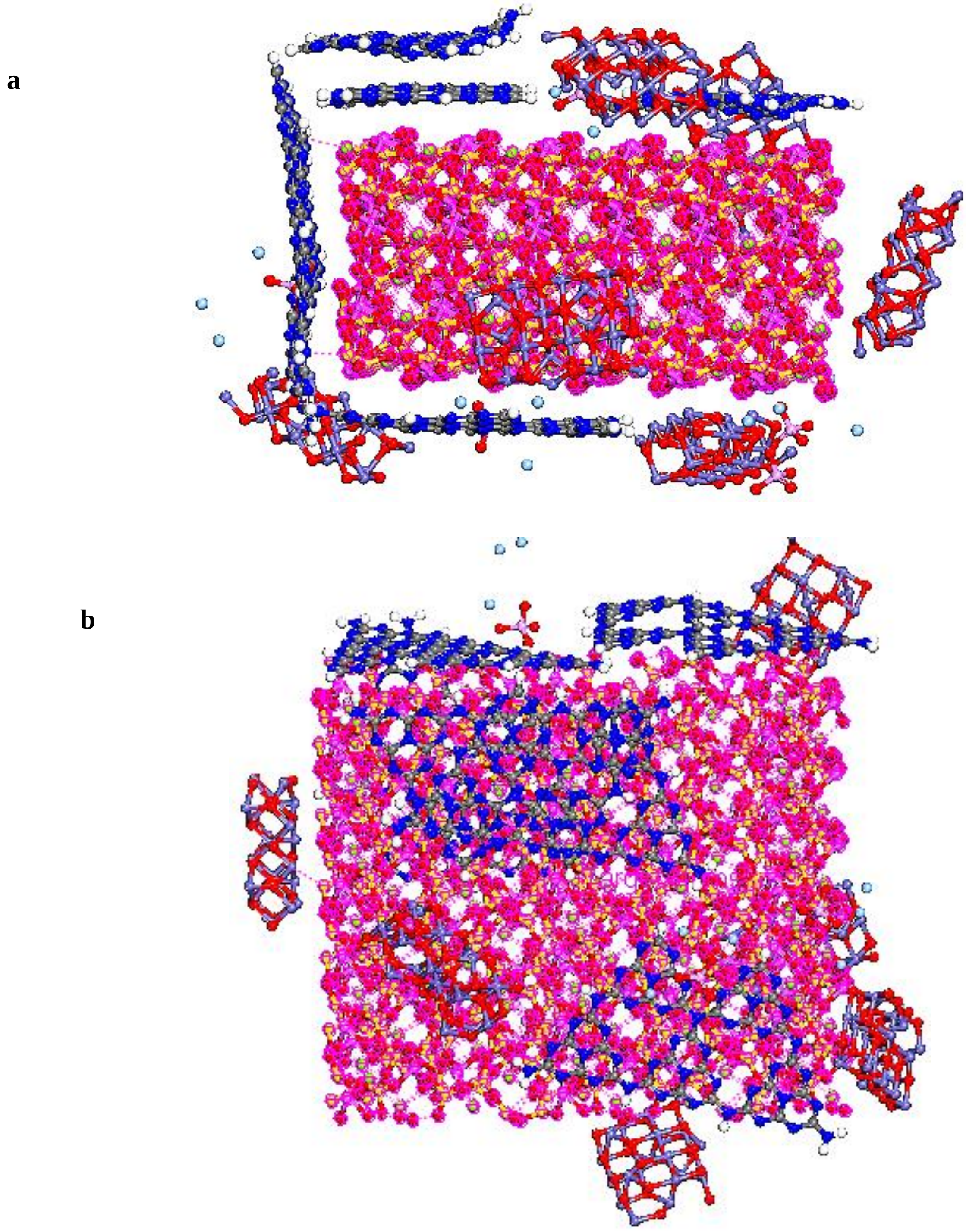

Figure. 17. (a and b); side and top views of the adsorption of 6 C_3N_4, Ag_3PO_4 and Fe_3O_4 molecules on Sep by adsorption locator module in Materials Studio 2017 software.

3.6. MG adsorption on Fe_3O_4/Ag_3PO_4@Sep by Monte Carlo adsorption locator simulation

In order to determine the most favorable adsorption geometry of MG on Fe_3O_4/Ag_3PO_4@Sep, 6 MG molecules were applied to adsorb on nano-composite in the gas phase by adsorption locator module and forcefield; universal in Materials Studio 2017 software (**Figures 18a-b**). The total energy of the system after the adsorption of MG (E_{ad}) on adsorbent was estimated about -436.229 kcal/mol as non-covalent interactions. The above adsorption energy reflected the thermodynamic stability of the whole adsorption system due to the negative value[50]. In other hand, the interaction was spontaneous and exothermic[51]. Based on the adsorption results, MG can be transported horizontally by van der Waals and electrostatic interactions as well as π-π stack between C_3N_4 and the delocalized π electron of MG, resulting dye elimination. The significant adsorption of the MG can be related π-π stack interactions by g-C_3N_4[52]. The computational studies revealed that all MG molecules on nanocomposite were the physisorption[53].

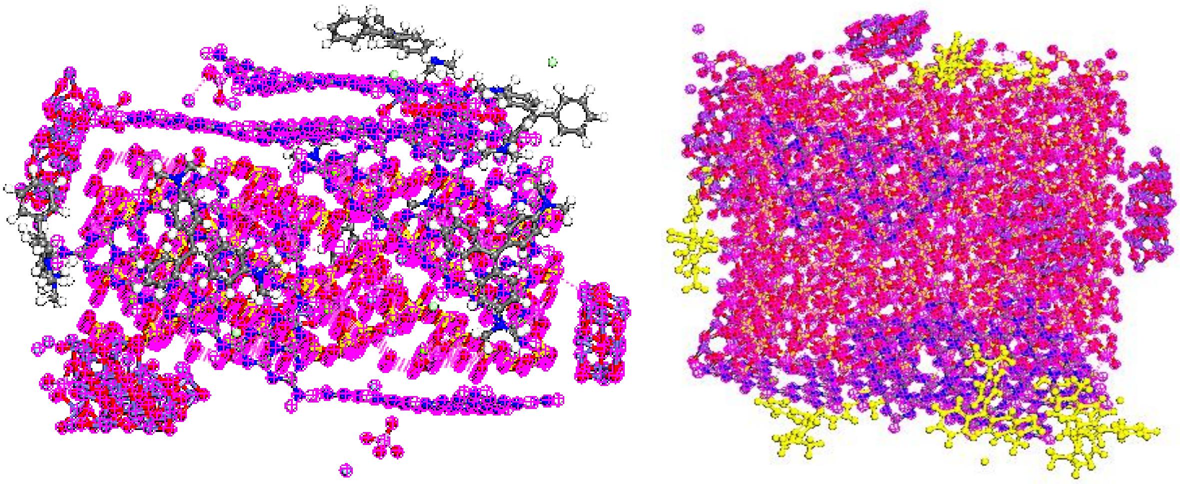

Figure. 18. (a and b); views of the adsorption of 6 MG molecules on Fe_3O_4/Ag_3PO_4@Sep by adsorption locator module in Materials Studio 2017 software.

Conclusion

In brief, a simple approch synthesis was used to produce g-$C_3N_4/Fe_3O_4/Ag_3PO_4$@Sep photocatalysts. The sepiolite clay was used as a support for the three semicounductors investigated Ag_3PO_4, g-C_3N_4 and Fe_3O_4. Based on the characterization results, Ag_3PO_4, g-C_3N_4 and Fe_3O_4 particles were formed on the sepiolite clay surface with intimate interactions occuring between them. The g-$C_3N_4/Fe_3O_4/Ag_3PO_4$@Sep magnetic nanocomposite in comparison to the others prepared photocatalysts, was found to be the most stable and it showed the higher activities for the MG degradation under sunlight irradiation. The photocatalytic enhancement of magnetic nanocomposite g-C_3N_4/Fe_3O_4/Ag_3PO_4@Sep to degrade organic molecules such as MG dye under solar light irradiation was attributed to the synergy effects occuring between the Ag_3PO_4, the g-C_3N_4 and the Fe_3O_4 nanoparticles, supported by the. sepiolite clay. The overall data indicate that the co-precipitation method, presented in this work, is a suitable approach to design and to synthesis new magnetic Z-scheme nanocomposite photocatalysts with enhanced stability and activity towards MG degradation. At the first, all structures were optimized by DFT-D in Material Studio 2017. The next stage, adsorption locator module was applied to adsorb Fe_3O_4 and Ag_3PO_4 on Sep, resulting exothermic system due to the high negative energy. Then, the adsorption mechanism of MG onto Fe_3O_4/Ag_3PO_4@Sep nano-composite was computationally investigated using MD through adsorption locator module. The result showed that MG was adsorbed through physisorption into nano-composit by using van der Waals and electrostatic interactions as well as π-π stack between C_3N_4 and MG. by MG adsorption, MG degradation can be happened by nanocomposite. This DFT simulation result confirmed experimental results.

Reference

1. Ouachtak, H., Akhouairi, S., Haounati, R., Addi, A.A., Jada, A., Taha, M.L., Douch, J.: 3,4-dihydroxybenzoic acid removal from water by goethite modified natural sand column fixed-bed: Experimental study and mathematical modeling. Desalin. Water Treat. 194, 439–449 (2020). https://doi.org/10.5004/dwt.2020.25562

2. Inyinbor, A.A., Bello, O.S., Fadiji, A.E., Inyinbor, H.E.: Threats from antibiotics: A serious environmental concern. J. Environ. Chem. Eng. 6, 784–793 (2018). https://doi.org/10.1016/j.jece.2017.12.056

3. Cheng, D., Ngo, H.H., Guo, W., Lee, D., Nghiem, D.L., Zhang, J., Liang, S., Varjani, S., Wang, J.: Performance of microbial fuel cell for treating swine wastewater containing sulfonamide antibiotics. Bioresour. Technol. 311, 123588 (2020). https://doi.org/10.1016/j.biortech.2020.123588

4. Schwarzenbach, R.P., Egli, T., Hofstetter, T.B., von Gunten, U., Wehrli, B.: Global Water Pollution and Human Health. Annu. Rev. Environ. Resour. 35, 109–136 (2010). https://doi.org/10.1146/annurev-environ-100809-125342

5. Samanta, P., Desai, A. V., Let, S., Ghosh, S.K.: Advanced Porous Materials for Sensing, Capture and Detoxification of Organic Pollutants toward Water Remediation. ACS Sustain. Chem. Eng. 7, 7456–7478 (2019). https://doi.org/10.1021/acssuschemeng.9b00155

6. Huang, Q., Song, S., Chen, Z., Hu, B., Chen, J., Wang, X.: Biochar-based materials and their applications in removal of organic contaminants from wastewater: state-of-the-art review. Biochar. 1, 45–73 (2019). https://doi.org/10.1007/s42773-019-00006-5

7. Nithya, R., Thirunavukkarasu, A., Sathya, A.B., Sivashankar, R.: Magnetic materials and magnetic separation of dyes from aqueous solutions: a review. Environ. Chem. Lett. 19, 1275–1294 (2021). https://doi.org/10.1007/s10311-020-01149-9

8. Largo, F., Haounati, R., Akhouairi, S., Ouachtak, H., El Haouti, R., El Guerdaoui, A., Hafid, N., Santos, D.M.F., Akbal, F., Kuleyin, A., Jada, A., Addi, A.A.: Adsorptive removal of both cationic and anionic dyes by using sepiolite clay mineral as adsorbent: Experimental and molecular dynamic simulation studies. J. Mol. Liq. 318, 114247 (2020). https://doi.org/10.1016/j.molliq.2020.114247

9. Haounati, R., Ouachtak, H., El Haouti, R., Akhouairi, S., Largo, F., Akbal, F., Benlhachemi, A., Jada, A., Addi, A.A.: Elaboration and properties of a new SDS/CTAB@Montmorillonite organoclay composite as a superb adsorbent for the removal of malachite green from aqueous solutions. Sep. Purif. Technol. 255, 117335 (2021). https://doi.org/10.1016/j.seppur.2020.117335

10. Yang, H., Yan, Z., Du, X., Bai, L., Yu, H., Ding, A., Li, G., Liang, H., Aminabhavi, T.M.: Removal of manganese from groundwater in the ripened sand filtration: Biological oxidation versus chemical auto-catalytic oxidation. Chem. Eng. J. 382, 123033 (2020). https://doi.org/10.1016/j.cej.2019.123033

11. Bouddouch, A., Amaterz, E., Bakiz, B., Taoufyq, A., Guinneton, F., Villain, S., Gavarri, J.R., Ezahri, M., Valmalette, J.C., Benlhachemi, A.: Role of thermal decomposition process in the photocatalytic or photoluminescence properties of BiPO4 polymorphs. Water Environ. Res. 1–14 (2020). https://doi.org/10.1002/wer.1340

12. Amaterz, E., Tara, A., Bouddouch, A., Taoufyq, A., Bakiz, B., Benlhachemi, A., Jbara, O.: Photo-electrochemical degradation of wastewaters containing organics catalysed by phosphate-based materials: a review. Rev. Environ. Sci. Biotechnol. 9, (2020).

https://doi.org/10.1007/s11157-020-09547-9

13. Haounati, R., El Guerdaoui, A., Ouachtak, H., El Haouti, R., Bouddouch, A., Hafid, N., Bakiz, B., Santos, D.M.F., Labd Taha, M., Jada, A., Ait Addi, A.: Design of direct Z-scheme superb magnetic nanocomposite photocatalyst Fe3O4/Ag3PO4@Sep for hazardous dye degradation. Sep. Purif. Technol. 277, 119399 (2021). https://doi.org/10.1016/j.seppur.2021.119399

14. Natarajan, S., Bajaj, H.C., Tayade, R.J.: Recent advances based on the synergetic effect of adsorption for removal of dyes from waste water using photocatalytic process. J. Environ. Sci. 65, 201–222 (2018)

15. Cai, T., Zeng, W., Liu, Y., Wang, L., Dong, W., Chen, H., Xia, X.: A promising inorganic-organic Z-scheme photocatalyst Ag3PO4/PDI supermolecule with enhanced photoactivity and photostability for environmental remediation. Appl. Catal. B Environ. 263, 118327 (2020). https://doi.org/10.1016/j.apcatb.2019.118327

16. Sulaeman, U., Suhendar, S., Diastuti, H., Riapanitra, A., Yin, S.: Design of Ag3PO4 for highly enhanced photocatalyst using hydroxyapatite as a source of phosphate ion. Solid State Sci. 86, 1–5 (2018)

17. Park, H., Son, N., Park, B.H., Liu, C., Joo, S.W., Kang, M.: Switching of a type I to an all-solid-state Z-scheme heterojunction by an electron mediator rGO bridge: 18.4% solar-to-hydrogen efficiency in n-ZnS/rGO/p-Bi2S3 ternary catalyst. Chem. Eng. J. 430, 133104 (2022). https://doi.org/10.1016/j.cej.2021.133104

18. Iqbal, W., Qiu, B., Lei, J., Wang, L., Zhang, J., Anpo, M.: One-step large-scale highly active g-C3N4 nanosheets for efficient sunlight-driven photocatalytic hydrogen production. Dalt. Trans. 46, 10678–10684 (2017). https://doi.org/10.1039/c7dt00849j

19. Paquin, F., Rivnay, J., Salleo, A., Stingelin, N., Silva, C.: Multi-phase semicrystalline microstructures drive exciton dissociation in neat plastic semiconductors. J. Mater. Chem. C. 3, 10715–10722 (2015). https://doi.org/10.1039/b000000x

20. Largo, F., Haounati, R., Akhouairi, S., Ouachtak, H., El Haouti, R., El Guerdaoui, A., Hafid, N., Santos, D.M.F., Akbal, F., Kuleyin, A., Jada, A., Addi, A.A.: Adsorptive removal of both cationic and anionic dyes by using sepiolite clay mineral as adsorbent: Experimental and molecular dynamic simulation studies. J. Mol. Liq. 318, (2020). https://doi.org/10.1016/j.molliq.2020.114247

21. Alvarado, M., Chianelli, R.C., Arrowood, R.M.: Computational Study of the Structure of a Sepiolite/Thioindigo Mayan Pigment. Bioinorg. Chem. Appl. 2012, 1–6 (2012). https://doi.org/10.1155/2012/672562

22. Feng, L., Liu, J., Abu-Hamdeh, N.H., Bezzina, S., Eshaghi Malekshah, R.: Molecular dynamics and quantum simulation of different cationic dyes removal from contaminated water using UiO-66 (Zr)-(COOH)2 metal–organic framework. J. Mol. Liq. 349, 118085 (2022). https://doi.org/10.1016/j.molliq.2021.118085

23. Heidari, Z., Pelalak, R., Malekshah, R.E., Pishnamazi, M., Marjani, A., Sarkar, S.M., Shirazian, S.: Molecular modeling investigation on mechanism of cationic dyes removal from aqueous solutions by mesoporous materials. J. Mol. Liq. 329, 115485 (2021). https://doi.org/10.1016/j.molliq.2021.115485

24. Jiang, F., Yan, T., Chen, H., Sun, A., Xu, C., Wang, X.: A g-C 3 N 4 -CdS composite catalyst with high visible-light-driven catalytic activity and photostability for methylene blue degradation. Appl. Surf. Sci. 295, 164–172 (2014). https://doi.org/10.1016/j.apsusc.2014.01.022

25. Yan, S.C., Li, Z.S., Zou, Z.G.: Photodegradation performance of g-C3N4 fabricated by directly heating melamine. Langmuir. 25, 10397–10401 (2009). https://doi.org/10.1021/la900923z

26. Dong, F., Zhao, Z., Xiong, T., Ni, Z., Zhang, W., Sun, Y., Ho, W.: In Situ Construction of g-C3N4 / g-C3N4 Metal-Free Heterojunction for Enhanced Visible Light Photocatalysis. (2013)

27. Zhu, Q., Zhang, Y., Lv, F., Chu, P.K., Ye, Z., Zhou, F.: Cuprous oxide created on sepiolite: Preparation, characterization, and photocatalytic activity in treatment of red water from 2,4,6-trinitrotoluene manufacturing. J. Hazard. Mater. 217–218, 11–18 (2012). https://doi.org/10.1016/j.jhazmat.2011.12.053

28. Zhang, Y., Wang, D., Zhang, G.: Photocatalytic degradation of organic contaminants by TiO2/sepiolite composites prepared at low temperature. Chem. Eng. J. 173, 1–10 (2011). https://doi.org/10.1016/j.cej.2010.11.028

29. Ahadpour Shal, A., Jafari, A.: Study of structural and magnetic properties of superparamagnetic Fe 3 O 4 -ZnO core-shell nanoparticles. J. Supercond. Nov. Magn. 27, 1531–1538 (2014). https://doi.org/10.1007/s10948-013-2469-9

30. Tan, L., Xu, J., Zhang, X., Hang, Z., Jia, Y., Wang, S.: Synthesis of g-C 3 N 4 /CeO 2 nanocomposites with improved catalytic activity on the thermal decomposition of ammonium perchlorate. Appl. Surf. Sci. 356, 447–453 (2015). https://doi.org/10.1016/j.apsusc.2015.08.078

31. Xu, H., Zhang, T., Gu, Y., Yan, X., Lu, N., Liu, H., Xu, Z., Xing, Y., Song, Y., Zhang, Z., Yang, M.: An electrochemical thrombin aptasensor based on the use of graphite-like C3N4 modified with silver nanoparticles. Microchim. Acta. 187, (2020). https://doi.org/10.1007/s00604-020-4111-4

32. Yang, L., Liu, X., Liu, Z., Wang, C., Liu, G., Li, Q., Feng, X.: Enhanced photocatalytic activity of g-C3N4 2D nanosheets through thermal exfoliation using dicyandiamide as precursor. Ceram. Int. 44, 20613–20619 (2018). https://doi.org/10.1016/j.ceramint.2018.06.105

33. Xu, M., Han, L., Dong, S.: Facile fabrication of highly efficient g-C3N4/Ag 2O heterostructured photocatalysts with enhanced visible-light photocatalytic activity. ACS Appl. Mater. Interfaces. 5, 12533–12540 (2013). https://doi.org/10.1021/am4038307

34. Zhu, P., Hu, M., Duan, M., Xie, L., Zhao, M.: High visible light response Z-scheme Ag3PO4 / g-C3N4 / ZnO composite photocatalyst for efficient degradation of tetracycline hydrochloride: Preparation, properties and mechanism. J. Alloys Compd. 840, 155714 (2020). https://doi.org/10.1016/j.jallcom.2020.155714

35. Yan, J., Song, Z., Wang, X., Xu, Y., Pu, W., Xu, H., Yuan, S., Li, H.: Enhanced photocatalytic activity of ternary Ag 3 PO 4 /GO/g-C 3 N 4 photocatalysts for Rhodamine B degradation under visible light radiation. Appl. Surf. Sci. 466, 70–77 (2019). https://doi.org/10.1016/j.apsusc.2018.09.234

36. Tomke, P.D., Rathod, V.K.: Facile fabrication of silver on magnetic nanocomposite (Fe3O4@Chitosan –AgNP nanocomposite) for catalytic reduction of anthropogenic pollutant and agricultural pathogens. Int. J. Biol. Macromol. 149, 989–999 (2020). https://doi.org/10.1016/j.ijbiomac.2020.01.183

37. Haounati, R., Alakhras, F., Ouachtak, H., Saleh, T.A., Al-Mazaideh, G., Alhajri, E., Jada, A., Hafid, N., Addi, A.A.: Synthesized of Zeolite@Ag2O Nanocomposite as Superb Stability Photocatalysis Toward Hazardous Rhodamine B Dye from Water.

Arab. J. Sci. Eng. (2022). https://doi.org/10.1007/s13369-022-06899-y

38. Schuhl, Y., Baussart, H., Delobel, R., Le Bras, M., Leroy, J.M., Gengembre, L., Grimblot, J.: Study of mixed-oxide catalysts containing bismuth, vanadium and antimony. Preparation, phase composition, spectroscopic characterization and catalytic oxidation of propene. J. Chem. Soc. Faraday Trans. 1 Phys. Chem. Condens. Phases. 79, 2055–2069 (1983). https://doi.org/10.1039/F19837902055

39. Arsalani, N., Bazazi, S., Abuali, M., Jodeyri, S.: A new method for preparing ZnO/CNT nanocomposites with enhanced photocatalytic degradation of malachite green under visible light. J. Photochem. Photobiol. A Chem. 389, 112207 (2020). https://doi.org/10.1016/j.jphotochem.2019.112207

40. Palareti, G., Legnani, C., Cosmi, B., Antonucci, E., Erba, N., Poli, D., Testa, S., Tosetto, A.: Comparison between different D-Dimer cutoff values to assess the individual risk of recurrent venous thromboembolism: Analysis of results obtained in the DULCIS study. Int. J. Lab. Hematol. 38, 42–49 (2016). https://doi.org/10.1111/ijlh.12426

41. Pradeeba, S.J., Sampath, K., Ramadevi, A.: Photo-catalytic degradations of methylene blue, malachite green and Bismarck brown using poly(azomethine)/TiO2 nanocomposite. Cluster Comput. 22, 3893–3909 (2019). https://doi.org/10.1007/s10586-018-2505-4

42. El-Hout, S.I., El-Sheikh, S.M., Gaber, A., Shawky, A., Ahmed, A.I.: Highly efficient sunlight-driven photocatalytic degradation of malachite green dye over reduced graphene oxide-supported CuS nanoparticles. J. Alloys Compd. 849, 156573 (2020). https://doi.org/10.1016/j.jallcom.2020.156573

43. Farhadian, M., Kazemzad, M.: Photocatalytic Degradation of Malachite Green by Magnetic Photocatalyst. Synth. React. Inorganic, Met. Nano-Metal Chem. 46, 458–463 (2016). https://doi.org/10.1080/15533174.2014.988802

44. Afshar, S., Samari Jahromi, H., Jafari, N., Ahmadi, Z., Hakamizadeh, M.: Degradation of malachite green oxalate by UV and visible lights irradiation using Pt/TiO2/SiO2 nanophotocatalyst. Sci. Iran. 18, 772–779 (2011). https://doi.org/10.1016/j.scient.2011.06.007

45. Jaiswal, A., Chattopadhayaya, M.C.: Removal of zinc ion from industrial effluents by

hydrotalcite-like compound. Desalin. Water Treat. 12, 127–132 (2009). https://doi.org/10.5004/dwt.2009.943

46. Manikandan, V.S., Harish, S., Archana, J., Navaneethan, M.: Fabrication of novel hybrid Z-Scheme WO3@g-C3N4@MWCNT nanostructure for photocatalytic degradation of tetracycline and the evaluation of antimicrobial activity. Chemosphere. 287, 132050 (2022). https://doi.org/10.1016/j.chemosphere.2021.132050

47. Zhou, Y., Zhang, Y., Lin, M., Long, J., Zhang, Z., Lin, H., Wu, J.C.S., Wang, X.: Monolayered Bi2WO6 nanosheets mimicking heterojunction interface with open surfaces for photocatalysis. Nat. Commun. 6, 1–8 (2015). https://doi.org/10.1038/ncomms9340

48. Song, H., Li, Y., Lou, Z., Xiao, M., Hu, L., Ye, Z., Zhu, L.: Synthesis of Fe-doped WO3 nanostructures with high visible-light-driven photocatalytic activities. Appl. Catal. B Environ. 166–167, 112–120 (2015). https://doi.org/10.1016/j.apcatb.2014.11.020

49. Wang, W.S., Du, H., Wang, R.X., Wen, T., Xu, A.W.: Heterostructured Ag3PO4/AgBr/Ag plasmonic photocatalyst with enhanced photocatalytic activity and stability under visible light. Nanoscale. 5, 3315–3321 (2013). https://doi.org/10.1039/c3nr00191a

50. Zhu, B., Zhang, L., Xu, D., Cheng, B., Yu, J.: Adsorption investigation of CO2 on g-C3N4 surface by DFT calculation. J. CO2 Util. 21, 327–335 (2017). https://doi.org/10.1016/j.jcou.2017.07.021

51. Gholivand, K., Alavinasab Ardebili, S.A., Mohammadpour, M., Eshaghi Malekshah, R., Hasannia, S., Onagh, B.: Preparation and examination of a scaffold based on hydroxylated polyphosphazene for tissue engineering: In vitro and in vivo studies. J. Appl. Polym. Sci. 139, 52179 (2022). https://doi.org/10.1002/app.52179

52. Zaboli, A., Raissi, H., Farzad, F., Hashemzadeh, H.: Assessment of adsorption behavior of 5-fluorouracil and pyrazinamide on carbon nitride and folic acid-conjugated carbon nitride nanosheets for targeting drug delivery. J. Mol. Liq. 301, 112435 (2020). https://doi.org/10.1016/j.molliq.2019.112435

53. Zhang, H., Ma, L., Ming, J., Liu, B., Zhao, Y., Hou, Y., Ding, Z., Xu, C., Zhang, Z., Long, J.: SC State Key Lab of Photocatalysis on Energy and Environment , College of

Chemistry ,. "Applied Catal. B, Environ. (2018). https://doi.org/10.1016/j.apcatb.2018.10.024